



## One hundred second bit-flip time in a two-photon dissipative oscillator

Camille Berdou, Anil Murani, Ulysse Reglade, William C. Smith, Marius Villiers, José Palomo, Michael Rosticher, A. Denis, Pascal Morfin, Matthieu Delbecq, et al.

### ► To cite this version:

Camille Berdou, Anil Murani, Ulysse Reglade, William C. Smith, Marius Villiers, et al.. One hundred second bit-flip time in a two-photon dissipative oscillator. PRX Quantum, 2023, 4 (2), pp.020350. 10.1103/PRXQuantum.4.020350 . hal-03662636

**HAL Id: hal-03662636**

**<https://hal.science/hal-03662636v1>**

Submitted on 27 Aug 2024

**HAL** is a multi-disciplinary open access archive for the deposit and dissemination of scientific research documents, whether they are published or not. The documents may come from teaching and research institutions in France or abroad, or from public or private research centers.

L'archive ouverte pluridisciplinaire **HAL**, est destinée au dépôt et à la diffusion de documents scientifiques de niveau recherche, publiés ou non, émanant des établissements d'enseignement et de recherche français ou étrangers, des laboratoires publics ou privés.



Distributed under a Creative Commons Attribution 4.0 International License

# One Hundred Second Bit-Flip Time in a Two-Photon Dissipative Oscillator

C. Berdou,<sup>1</sup> A. Murani,<sup>2</sup> U. Réglade,<sup>1,2</sup> W.C. Smith,<sup>1</sup> M. Villiers,<sup>1</sup> J. Palomo,<sup>1</sup> M. Rosticher,<sup>1</sup> A. Denis,<sup>1</sup> P. Morfin,<sup>1</sup> M. Delbecq,<sup>1</sup> T. Kontos,<sup>1</sup> N. Pankratova,<sup>1</sup> F. Rautschke<sup>2</sup>,<sup>2</sup> T. Peronnin,<sup>2</sup> L.-A. Sellem<sup>2</sup>,<sup>1</sup> P. Rouchon,<sup>1</sup> A. Sarlette,<sup>1</sup> M. Mirrahimi,<sup>1</sup> P. Campagne-Ibarcq,<sup>1</sup> S. Jezouin,<sup>2</sup> R. Lescanne<sup>2</sup>,<sup>2</sup> and Z. Leghtas<sup>1,\*</sup>

<sup>1</sup>Laboratoire de Physique de l'Ecole normale supérieure, Centre Automatique et Systèmes, Mines Paris, Inria, ENS-PSL, Université PSL, CNRS, Sorbonne Université, Paris, France

<sup>2</sup>Alice & Bob, 53 Bd du Général Martial Valin, Paris 75015, France



(Received 20 May 2022; revised 25 January 2023; accepted 5 May 2023; published 23 June 2023)

Bistable dynamical systems are widely employed to robustly encode classical bits of information. However, they owe their robustness to inherent losses, making them unsuitable to encode quantum information. Surprisingly, there exists a loss mechanism, known as two-photon dissipation, that provides stability without inducing decoherence. An oscillator exchanging pairs of photons with its environment is expected to reach macroscopic bit-flip times between dynamical states containing only a handful of photons. However, previous implementations have observed bit-flip times saturating in the millisecond range. In this experiment, we design a superconducting resonator endowed with two-photon dissipation, and free of all suspected sources of instabilities and inessential ancillary systems. We attain bit-flip times exceeding 100 s in between states containing about 40 photons. Although a full quantum model is necessary to explain our data, the preparation of coherent superposition states remains inaccessible. This experiment demonstrates that macroscopic bit-flip times are attainable with mesoscopic photon numbers in a two-photon dissipative oscillator.

DOI: [10.1103/PRXQuantum.4.020350](https://doi.org/10.1103/PRXQuantum.4.020350)

## I. INTRODUCTION

Bistable dynamical systems [1,2] play a central role in near-quantum-limited amplification [3,4] and ultralow power classical logic [5,6]. They are particularly well suited for the latter since the two states of a classical bit are encoded in each dynamical state containing only a handful of excitations. These two states are separated by a potential barrier, and friction dampens erroneous diffusion between states, resulting in macroscopic bit-flip times [7]. Promoting these systems to robustly encode quantum information is difficult. Indeed, the phenomenon that stabilizes each dynamical state, namely friction, is also responsible for wiping out coherent quantum superpositions.

In recent years, a growing interest has focused on a new type of friction known as two-photon dissipation [8,9]. Surprisingly, this mechanism stabilizes two dynamical

states without affecting their quantum superposition. This sparked the idea of the cat qubit [10], where information is encoded in superpositions of coherent states of amplitude denoted  $\pm\alpha$ , stabilized by two-photon dissipation. Increasing the number of photons  $\bar{n} = |\alpha|^2$  in these two steady states has two opposing effects [11]. On the one hand, their distinguishability by an inevitably coupled uncontrolled environment increases linearly with  $\bar{n}$ . This results in a linear increase of the phase-flip error rate. Therefore, for this system to be suitable for quantum information processing, it must operate at low photon number. On the other hand, as soon as their separation exceeds their vacuum fluctuations, that is  $|\alpha - (-\alpha)|^2 = 4\bar{n} > 1$ , their wave-function overlap exponentially decreases. This is notoriously efficient at preventing bit flips caused by diffusive (i.e., local) errors that only locally spread states out in phase space. Most known noise sources, such as dielectric or charge noise [12], are local. In contrast, non-diffusive (i.e., nonlocal) errors induce large excursions in phase space, resulting in bit flips. Well-known examples are high-energy particle impacts on superconducting chips [13] and errors propagating through ancillas [14]. The bit-flip time is therefore expected to increase exponentially with  $\bar{n}$ , until hitting a plateau set by a nondiffusive error mechanism.

\*zaki.leghtas@ens.fr

Published by the American Physical Society under the terms of the [Creative Commons Attribution 4.0 International](https://creativecommons.org/licenses/by/4.0/) license. Further distribution of this work must maintain attribution to the author(s) and the published article's title, journal citation, and DOI.

Previous experiments implementing cat qubits have observed the linear increase of phase flips and exponential suppression of bit-flips [11], before hitting a plateau in the millisecond range [11,15]. The suspected nondiffusive error mechanisms at play were a thermally excited strongly coupled ancillary qubit [11], a combination of thermal excitation and Kerr nonlinearity in the oscillator [15,16], and possible dynamical instabilities [17–19].

In this work we find that by removing all suspected sources of dynamical instabilities and ancillary systems that could propagate nondiffusive errors, the bit-flip time plateaus at 100 s for states containing about 40 photons. Since quantum fluctuations play a central role in this experiment, a full quantum model is necessary to explain our data. Our design choices came at the cost of a two-photon exchange rate dominated by single-photon loss hence losing our ability to prepare quantum superposition states and measure the phase-flip rate. This experiment proves that two-photon dissipation is capable of attaining macroscopic bit-flip times with mesoscopic photon numbers.

## II. THE TWO-PHOTON DISSIPATIVE OSCILLATOR

An oscillator exchanging pairs of photons with its environment in addition to usual energy relaxation (see Fig. 1) is modeled by the following Hamiltonian and loss operators:

$$H_2/\hbar = i\epsilon_2 a^{\dagger 2} - i\epsilon_2^* a^2, \quad L_2 = \sqrt{\kappa_2} a^2, \quad L_1 = \sqrt{\kappa_a} a, \quad (1)$$

where  $a$  is the annihilation operator of the mode referred to as the memory,  $\epsilon_2$  is the two-photon injection rate,  $\kappa_2$  the two-photon loss rate, and  $\kappa_a$  is the energy damping rate. The loss operators  $L = L_{1,2}$  enter the Lindblad master equation for the density matrix  $\rho$  through the Lindblad operator  $\mathcal{D}[L]\rho = L\rho L^\dagger - \frac{1}{2}L^\dagger L\rho - \frac{1}{2}\rho L^\dagger L$ . When the two-photon injection rate dominates the damping rate, two metastable pointer states emerge:

$$|0\rangle_\alpha = |+\alpha\rangle + \mathcal{O}(e^{-2|\alpha|^2}), \quad |1\rangle_\alpha = |-\alpha\rangle + \mathcal{O}(e^{-2|\alpha|^2}),$$

where  $|\alpha\rangle$  is a coherent state with complex amplitude  $\alpha$ , verifying  $\alpha^2 = (2/\kappa_2)(\epsilon_2 - \kappa_a/4)$  if  $\epsilon_2 > \kappa_a/4$ , and  $\alpha^2 = 0$  otherwise.

The two-photon dissipation mechanism is engineered by implementing a two-to-one photon exchange interaction with a dissipative mode referred to as the buffer [9], modeled by the Hamiltonian

$$H_{ab}/\hbar = g_2^* a^2 b^\dagger + g_2 a^{\dagger 2} b - \epsilon_d b^\dagger - \epsilon_d^* b, \quad (2)$$

where  $b$  is the annihilation operator of the buffer,  $g_2$  is the two-to-one photon coupling rate, and  $\epsilon_d$  the buffer

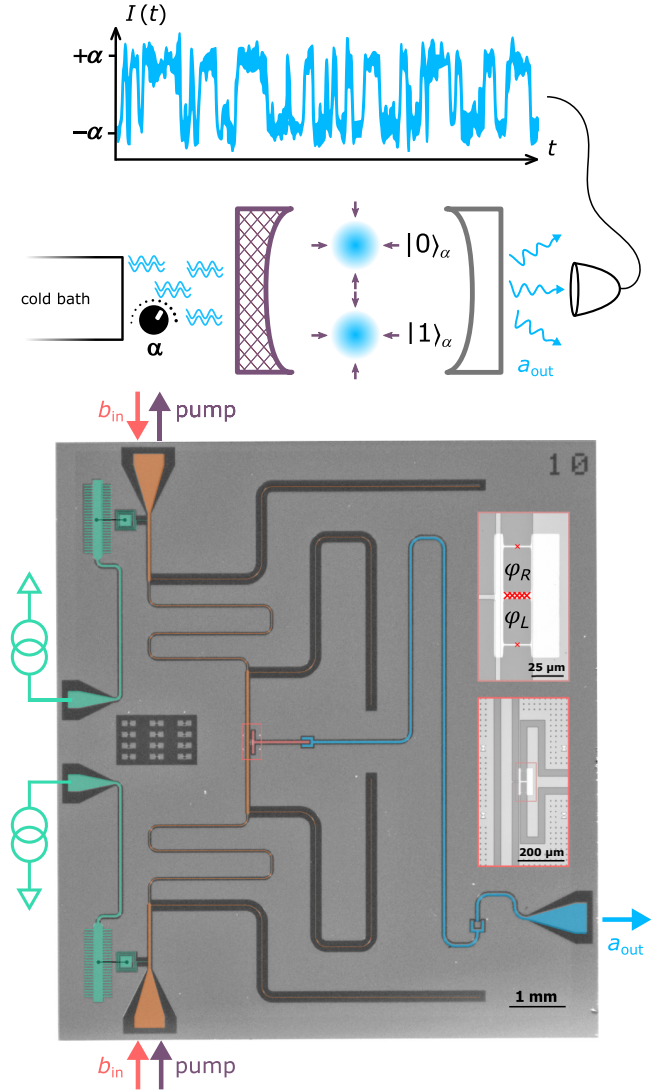


FIG. 1. (Top) Principle of the experiment. A cavity is endowed with a special mechanism (dashed left mirror) that exchanges pairs of photons (blue double waves) at variable intensity (control knob) with a cold bath. Two metastable pointer states emerge, represented by the blue distributions centered around amplitudes  $\pm\alpha$ . The resemblance of the steady states to these circular Gaussian distributions is valid in the limit of large  $|\alpha|$ . A fraction of the cavity field (blue waves) escapes through the weakly transmissive mirror and is collected by our heterodyne detector. By monitoring the signal over time, we track individual trajectories undergoing bit flips (blue time trace). (Bottom) False-color optical micrograph of the experimental superconducting circuit in a coplanar waveguide geometry. The cavity is a  $\lambda/2$  resonator (blue) that radiates a field  $a_{\text{out}}$  through a weakly coupled 50- $\Omega$  port. It also couples to a two-photon exchange device composed of a buffer mode (red) shunted to ground through an asymmetrically threaded SQUID (ATS) as emphasized in the insets. dc currents enter through on-chip bias tees (green) and impose phase biases  $\varphi_{L,R}$ . A differential pump (purple arrows) and a common buffer drive (red arrows) are channeled through filtered transmission lines (orange).

drive amplitude. In the limit where the buffer energy decay rate  $\kappa_b$  is larger than  $|g_2|$ , we recover Eq. (1) with  $\kappa_2 = 4|g_2|^2/\kappa_b$  and  $\epsilon_2 = 2g_2\epsilon_d/\kappa_b$  [9].

### III. CIRCUIT DESIGN

Our two-photon dissipative oscillator is implemented in a circuit quantum electrodynamics coplanar waveguide architecture (see Fig. 1). The memory mode is the fundamental mode of a  $\lambda/2$  resonator. We measure coupling and internal loss rates  $\kappa_a^c/2\pi = 40$  kHz and  $\kappa_a^i/2\pi = 18$  kHz. In order to minimize dielectric losses [12], we target the relatively low frequency of  $\omega_a/2\pi = 4.0457$  GHz. A thermal population of about 1% is measured on a twin sample using a transmon (see Appendix D 6). An undesired side effect of coupling the memory to a lossy mode—the buffer—is to increase the decay rate of the memory due to the Purcell effect. To prevent this, we design a stop-band filter centered at the memory frequency, consisting of three  $\lambda/4$  sections [20] on both routes linking the memory to its cold bath. The buffer mode consists of a metallic plate of charging energy  $E_C/h = 73$  MHz shunted to ground through an asymmetrically threaded superconducting quantum interference device (SQUID ATS) [17]. The ATS is formed by two Josephson junctions in a loop—each of Josephson energy  $E_J/h = 37$  GHz—split in its center by an inductance made of five junctions of total inductive energy  $E_L/h = 62$  GHz. This layout defines two loops that can be biased in dc flux  $\phi_{L,R}$ . We can hence independently control the common and differential flux through the ATS:  $\varphi_\Sigma = \frac{1}{2}(\varphi_L + \varphi_R)$  and  $\varphi_\Delta = \frac{1}{2}(\varphi_L - \varphi_R)$ . rf signals are routed to the ATS through a  $180^\circ$  hybrid coupler. The buffer drive propagates in phase through both arms of the two-photon exchange apparatus. When reaching the ATS, these waves combine, inducing currents in the inductance and thereby driving the buffer mode. On the other hand, the pump propagates with opposite phases, inducing common flux in the ATS.

In the process of choosing the ATS parameters, we are guided by the intuition that dynamical instabilities would be avoided in a system with  $2E_J/E_L \lesssim 1$  [18,19]. However, this criterion needs to be balanced with the requirement of large  $g_2$ . In this experiment, we favor stability over coupling strength and choose  $2E_J/E_L = 1.2$ , a factor of 3.3 smaller than our previous implementation [17]. Moreover, we engineer a weak hybridization between the memory and buffer mode in order to minimize undesired nonlinear couplings such as the Kerr effect, with a rate estimated below 1 Hz.

Previous experiments constructed the Wigner distribution of the memory field through a nonlinear coupling to a transmon qubit and its readout resonator [17]. However, the finite thermal occupation of the transmon is suspected to limit the bit-flip time to the millisecond range. Instead, we monitor our memory through a minimally

invasive detection tool: a weakly coupled transmission line connected to a traveling-wave paramagnetic amplifier (TWPA). The coupling is weak enough so that this added leakage channel only slightly decreases the total quality factor but has the advantage of not inducing any additional nonlinear couplings to a lossy ancillary system.

### IV. EXPERIMENT CALIBRATION

The ATS contributes a nonlinear potential energy of the form  $U_{\varphi_\Sigma, \varphi_\Delta}(\varphi) = \frac{1}{2}E_L\varphi^2 - 2E_J\cos(\varphi_\Sigma)\cos(\varphi + \varphi_\Delta)$ , where  $\varphi$  is the phase drop across the central inductance [17]. The buffer and memory modes hybridize through their capacitive coupling, and hence to the lowest order of their hybridization strength  $v$ , we have  $\varphi = \varphi_b(b + b^\dagger + v(a + a^\dagger))$ , where the buffer zero-point phase fluctuations verifies  $\varphi_b = (2E_C/E_L)^{1/4}$  [21]. We operate the ATS at  $\varphi_\Sigma = -\pi/2 + \varepsilon_p\cos(\omega_p t)$ , and  $\varphi_\Delta = \pi/2$ . At this operating point the buffer resonates at  $\omega_b/2\pi = 6.1273$  GHz with an energy decay rate  $\kappa_b/2\pi = 16$  MHz. By tuning the pump frequency at  $\omega_p = 2\omega_a - \omega_b$  and driving the buffer mode at  $\omega_d = \omega_b$ , we synthesize the Hamiltonian of Eq. (2), with  $\hbar g_2 = -\frac{1}{2}E_J\varepsilon_p v^2 \varphi_b^3$ .

We start the experiment by measuring the buffer-mode frequency map as a function of the two dc currents. Conveniently, the desired operating point  $(\varphi_\Sigma, \varphi_\Delta) = (-\pi/2, \pi/2)$  is easily recognizable since it corresponds to a saddle point of this map. Consequently, the buffer and memory modes are first order insensitive to flux noise.

The next step is to activate the rf pump and buffer drive. We pick the largest pump power that does not deteriorate the buffer and memory modes' spectra. The modes' frequencies are Stark shifted in the presence of this strong pump. Therefore, a precise calibration of the pump and drive frequencies is required to rigorously verify the frequency-matching conditions:  $\omega_p = 2\omega_a - \omega_d$ , and  $\omega_d = \omega_b$ . To this end, we acquire the memory-mode fluorescence as a function of detunings from these matching conditions. As the drive amplitude  $\epsilon_d$  is increased, the region over which the drive and pump combine to populate the memory expands around the frequency-matching point [see Fig. 2(a)]. For the remainder of the experiment, we place ourselves at the center of these regions (colloquially referred to as diamonds).

We calibrate the number of photons in the memory by measuring  $\overline{I^2 + Q^2}$  (See Appendix D) as a function of the drive amplitude, where  $I$  and  $Q$  are the in-phase and out-of-phase quadratures of the radiated field acquired over an integration time  $T_m$  [see Fig. 2(b)]. Three notable features are apparent. First, in the limit of strong drives, the radiated energy scales linearly with the drive amplitude, a signature of the conversion of one buffer photon to two memory photons. This is in stark contrast with the common quadratic scaling for a driven harmonic oscillator. Moreover, the offset of this asymptote from the origin



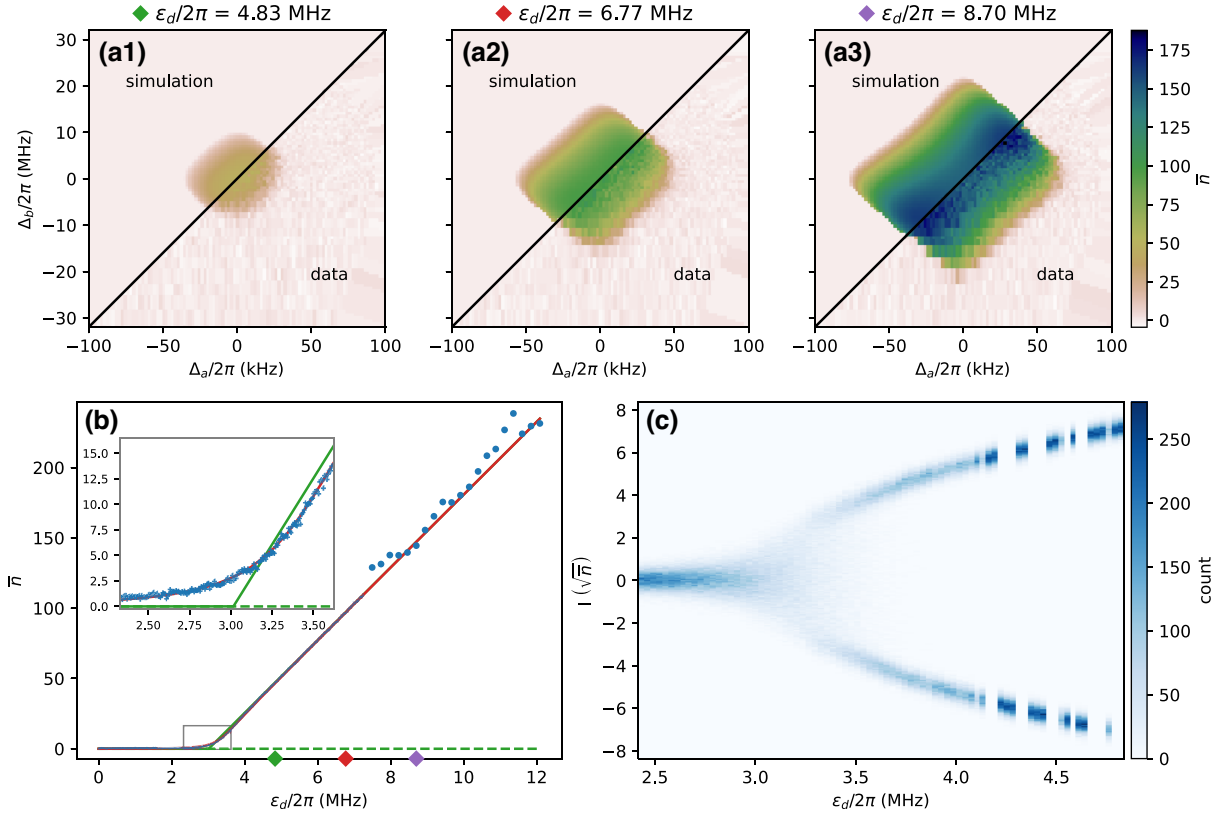


FIG. 2. Emergence of two metastable pointer states from a nonlinear dissipative phase transition. (a1)–(a3) Radiated energy from the memory mode in units of circulating photon number (color) as a function of the detuning from the frequency-matching condition  $\Delta_a = \frac{1}{2}(\omega_p - (2\omega_a - \omega_d))$  (x axis), and the detuning from the buffer resonance  $\Delta_b = \omega_d - \omega_b$  (y axis). We denote  $\omega_{a,b,p,d}$  the memory, buffer, pump, and drive angular frequencies, respectively. Both data and semiclassical numerical simulations are shown in different regions of each panel corresponding to the specified drive amplitude  $\epsilon_d$ . (b) Radiated energy from the memory in units of circulating photon number (y axis) at  $\Delta_a = \Delta_b = 0$  as a function of the drive amplitude (x axis). The data correspond to an integration time of  $10 \mu\text{s}$  with single averaging (circles) and 10 000 averages (crosses). A semiclassical model (green solid line) captures the appearance of a critical point around  $\epsilon_d/2\pi \approx 3$  MHz above which the vacuum state becomes unstable (green dashed line). A full quantum model (red solid line) is necessary to capture the curvature at the critical point, as emphasized by the enlargement in the inset panel. (c) Histogram (color) of the  $I$  quadrature integrated over 1 ms of the field radiated by the memory (y axis) in units of the square root of circulating photon number as a function of the drive amplitude (x axis). Passed the critical point, the memory field transits from the vacuum into two metastable pointer states.

excludes the Kerr effect as the underlying process (See Appendix B 7). Second, the output power is close to zero up until a critical drive amplitude, reminiscent of a nonlinear dissipative phase transition [22]. This transition occurs when the two-photon injection rate overcomes the memory losses, setting the scale for the product  $\epsilon_d g_2$  to its value at the critical point  $\epsilon_d g_2 = \kappa_a \kappa_b / 8$ . Furthermore, we compute the classical dependence of  $\bar{n} g_2^2$  on  $\epsilon_d g_2$ , demonstrating that it is invariant under a change of  $g_2$  (see Appendix D). Importantly, quantum fluctuations blur the transition out of vacuum resulting in a nonscale invariant curvature, a striking deviation from the sharp transition expected in the classical regime. A full quantum model is necessary to capture this third notable feature, from which we extract the key parameter  $g_2/2\pi = 39$  kHz, and deduce  $\kappa_2/2\pi = 370$  Hz and  $\bar{n}$  for every  $\epsilon_d$ . This places our experiment in

the regime where  $\kappa_a/\kappa_2 = 150 \gg 1$ . In the future we will increase the hybridization factor  $\nu$  to enter the regime suitable for a qubit implementation: where the two-photon exchange rate largely dominates the cavity losses. Finally, with the photon number calibration in hand, the measurement records  $I$  and  $Q$  are rescaled to, respectively, coincide with a measurement of  $(a + a^\dagger)/2$  and  $(a - a^\dagger)/2i$ .

In fact, the observed phase transition corresponds to a spontaneous symmetry breaking, where the cavity field adopts two opposite phases (or any quantum superposition of the two in the absence of single-photon loss). We observe the emergence of these two phases by continuously acquiring, for each drive amplitude, 10 000 times the  $I$  quadrature of the radiated field integrated over  $T_m = 1$  ms, for a total measurement duration of 10 s [see Fig. 2(c)]. For the lowest drive amplitudes ( $\epsilon_d/2\pi \lesssim 2.7$

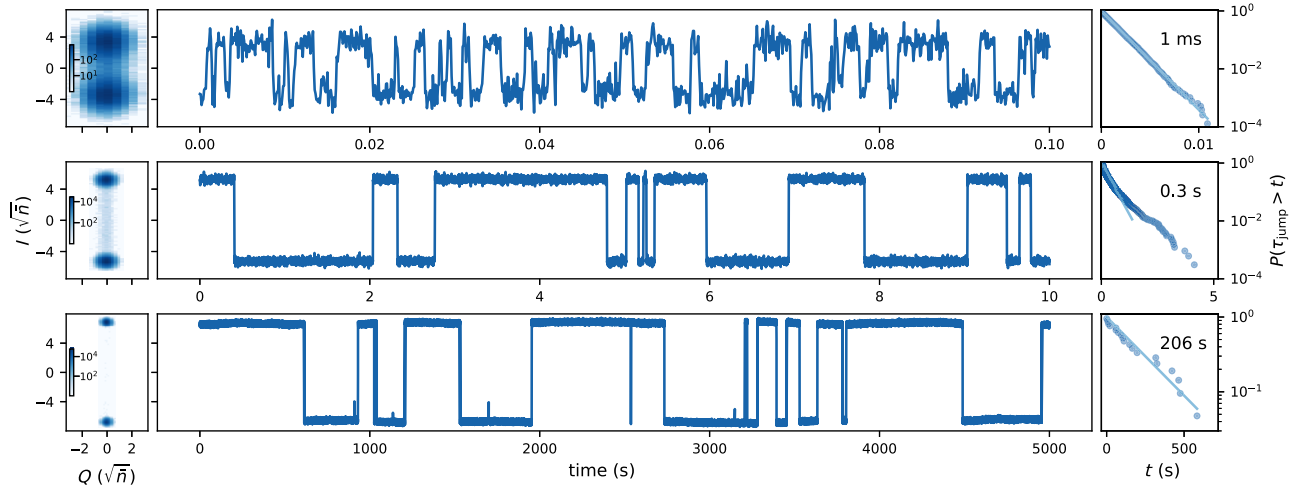


FIG. 3. Real-time oscillator dynamics revealed by individual trajectories. For photon numbers  $\bar{n} = 11, 28, 43$  (top, middle, bottom), we, respectively, set the integration time to  $T_m = 0.1, 1, 5$  ms and the total measurement duration to  $T_{\text{tot}} = 10, 1000, 5000$  s. (Left) Histogram of the  $(I, Q)$  quadratures of the radiated field. The narrowing of the distributions from top to bottom is due to the increasing integration time  $T_m$ . (Center) Trajectory of the  $I$  quadrature as a function of time cropped from the full dataset. (Right) Cumulative distribution function of the stochastic time interval  $\tau_{\text{jump}}$  in between two consecutive jumps. Its average value, that defines the bit-flip time  $T_{\text{bit-flip}}$ , is printed on each panel. The solid lines represent the cumulative distribution for Poisson's statistics  $e^{-t/T_{\text{bit-flip}}}$ .

MHz), the cavity state remains in the vacuum, as signaled by the Gaussian distribution centered at  $I = 0$ . This distribution then broadens around the critical point ( $2.7 \text{ MHz} \lesssim \epsilon_d/2\pi \lesssim 3.5 \text{ MHz}$ ), due to the significant overlap of the distributions of states  $|\pm\alpha\rangle$  at small  $\alpha$  and the multiple flips in between during the acquisition time  $T_m = 1$  ms. For ( $3.5 \text{ MHz} \lesssim \epsilon_d/2\pi \lesssim 4 \text{ MHz}$ ), the two states are well resolved, and their approximately equal weights hint towards a bit-flip time larger than the acquisition time of 1 ms and smaller than the full experiment duration of 10 s. For  $\epsilon_d/2\pi \gtrsim 4 \text{ MHz}$ , the field stays pinned to one of the two computational states, hinting towards bit-flip times exceeding 10 s.

## V. TRAJECTORIES AND BIT-FLIP TIMES

We access the dynamics of the memory by tracking individual trajectories over time (see Fig. 3). For each trajectory, we set the drive amplitude at a fixed value  $\epsilon_d$ , and record the  $I$  quadrature of the radiated field. In order to resolve quantum jumps, we set the integration time  $T_m$  to be simultaneously smaller than the bit-flip time and sufficiently large to average out the heterodyne detection noise. To capture the statistical properties of each trajectory, we plot the cumulative distribution function of the interval between two consecutive jumps, denoted  $\tau_{\text{jump}}$ . It shows approximately an exponential law, revealing an underlying Poisson process. The average of  $\tau_{\text{jump}}$ , that defines the bit-flip time, undergoes a spectacular increase from 1 ms to 0.3 to 206 s for an increase of photon number  $\bar{n}$  from 11 to 28 to 43. With respect to the bare cavity lifetime of  $2.7 \mu\text{s}$ , this represents a  $10^8$  increase of the bit-flip time, and

(although inaccessible with our measurement scheme) an estimated  $2 \times 43 = 86$  fold decrease of the phase-flip time.

We quantify the scaling of the bit-flip time with the photon number by repeating the trajectory acquisition procedure for multiple drive amplitudes. From each trajectory we extract the bit-flip time and the corresponding photon number, and display them in Fig. 4. We observe two distinct regimes. For  $\bar{n} \lesssim 40$ , the bit-flip time rises exponentially multiplying by a factor of about 1.4 for every

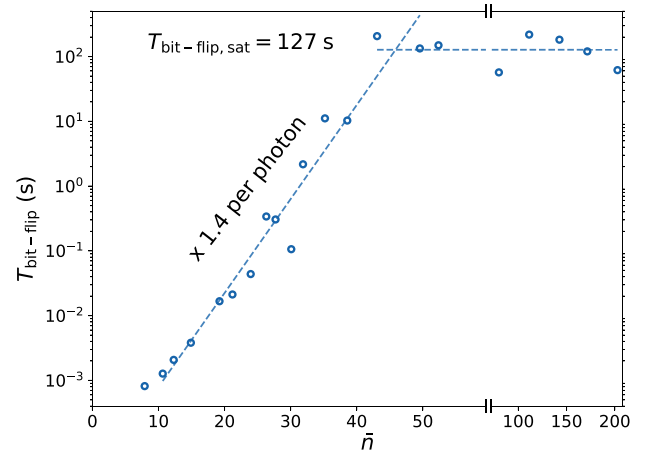


FIG. 4. Exponential suppression of bit flips. The bit-flip time ( $y$  axis, log scale) is measured (open circles) as a function of the number of photons contained in the pointer states  $|0/1\rangle_\alpha$  ( $x$  axis). The bit-flip time increases exponentially, multiplying by 1.4 per photon (tilted dashed line) before saturating at approximately 127 s (horizontal dashed line).

added photon. In theory, in the limit where  $\kappa_a/\kappa_2 \ll 1$ , this factor would approach  $e^2 \sim 7.4$  [10]. In this experiment we favored stability over coupling strength, placing ourselves in the opposite regime  $\kappa_a/\kappa_2 \sim 150$ . Consequently, the scaling factor is expected to be significantly reduced and develop a weak dependence on  $\bar{n}$ , as visible in our data, and confirmed by numerical simulations (see Appendix E). For  $\bar{n} \gtrsim 40$  photons, the bit-flip time saturates in the 100-s range. Although the origin of this saturation is yet to be established, its timescale is compatible with the measured rate of highly correlated errors in a large array of qubits [13], possibly due to high-energy particle impacts [23,24].

## VI. DISCUSSION

In this section we discuss how the results of this experiment may advance the implementation of cat qubits, where bit flips are expected to be autonomously and continuously protected over macroscopic timescales, and phase flips would be corrected in a one-dimensional repetition code [25,26], which lightens the hardware requirements over two-dimensional surface codes [27,28]. Previous experimental implementations of cat qubits have observed bit-flip times plateau in the millisecond range [11,15]. This experiment has shown that by circumventing all suspected sources of dynamical instabilities, and removing the transmon qubit usually employed for quantum tomography, the bit-flip time rises exponentially with photon number for an extra 6 orders of magnitude before hitting a plateau at 100 s.

This work therefore points towards a transmon-free cat-qubit architecture. The next milestone will be that the ability to prepare and measure quantum superposition states—absent in this experiment—is recovered. First, the two-photon dissipation rate  $\kappa_2$  needs to be increased until it dominates all loss mechanisms. Since  $\kappa_2$  depends on the fourth power of the memory phase fluctuations across the ATS, we expect that increasing the buffer-memory hybridization by a factor of 10, would increase  $\kappa_2$  by 4 orders of magnitude, thereby reaching the MHz range and largely superseding  $\kappa_a$ . Second and most importantly, the absence of the transmon does not jeopardize full quantum tomography of the memory mode. Indeed, the ATS mediates a variety of nonlinear interactions between the memory and the buffer, that when appropriately parametrically pumped, could map memory quantum observables onto the buffer output field.

## VII. CONCLUSION

In conclusion, we measure timescales of order 100 s for bit flips between pointer states of a two-photon dissipative oscillator containing about 40 photons. To reach these macroscopic bit-flip times with mesoscopic photon numbers, we design a two-photon exchange circuit

in a regime expected to circumvent dynamical instabilities, and replaced the transmon qubit usually used for tomography by a minimally invasive detection tool that collects the oscillator’s radiated field. Our experiment thus puts a scale on the bit-flip times attainable with two-photon dissipation, a necessary mechanism for quantum information processing with cat qubits [16]. Future work could be to uncover the phenomena causing these bit-flip events [23,24,29] by monitoring oscillator trajectories over timescales of days or weeks. Also, gradually increasing the two-photon exchange rate so that it supersedes all loss mechanisms would lead to the regime suitable for the cat qubit where quantum superposition states can be prepared and measured, thereby paving the way towards fully protected chains of cat qubits [25,26].

## ACKNOWLEDGMENTS

We thank Lincoln Labs for providing a Josephson traveling-wave parametric amplifier. The devices are fabricated within the consortium Salle Blanche Paris Centre. We thank Jean-Loup Smirr and the Collège de France for providing nanofabrication facilities. This work is supported by the QuantERA Grant QuCOS, by ANR 19-QUAN-0006-04. Z.L. acknowledges support from ANR project ENDURANCE, and EMERGENCE Grant ENDURANCE of Ville de Paris. This work is supported by the Paris Île-de-France Region in the framework of DIM SIRTEQ. This project has received funding from the European Research Council (ERC) under the European Union’s Horizon 2020 research and innovation programme (Grant Agreements No. 851740 and No. 884762). This work is funded by the French Grants ANR-22-PETQ-0003 and ANR-22-PETQ-0006 under the “France 2030” plan.

## AUTHOR CONTRIBUTIONS

C.B. simulated and fabricated the device. C.B., A.M., and Z.L. measured the device. C.B., A.M., U.R., R.L., S.J., and Z.L. analyzed the data and co-wrote the manuscript with input from all authors. W.C.S., M.V., A.D., and P.M. designed the sample holder. Support is provided by J.P., N.P., and M.R. for nanofabrication, M.D., T.K., R.L., and T.P. for experimental tools, F.R. for microwave engineering, L.A.S., P.R., A.S., and M.M. for theory. Z.L., R.L., P.C., and M.M. conceived the experiment.

## APPENDIX A: DEVICE FABRICATION AND WIRING

### 1. Wafer preparation

We sputter 120 nm of Nb on a 2-in. intrinsic silicon wafer, with a 280  $\mu\text{m}$  thickness and a resistivity larger than 10 k $\Omega\text{cm}$ . We fabricate twelve 10  $\times$  11 mm chips on the same wafer. We dice the individual chips at the end of the

fabrication process and select the sample that is best suited for the experiment.

## 2. Circuit patterning

We pattern the large features of the circuit ( $>5 \mu\text{m}$ ) using laser lithography. We spin positive resist (S1805), expose the pattern, then develop in MF319 for 1 min and rinse in deionized (DI) water for 1 min. The wafer is then etched in a reactive ion-etching machine with a SF6 plasma and a 10-s overetch. A 30-min liftoff step follows in a  $50^\circ\text{C}$  acetone bath with sonication. Finally, the sample is rinsed in isopropyl alcohol (IPA) for 1 min, blow dried, and cleaned in an  $\text{O}_2$  plasma for 20 s, thus stripping residual organic contaminants.

## 3. Junction patterning

Our Josephson junctions are fabricated from Dolan bridges patterned with electron-beam ( $e$ -beam) lithography. We spin two layers of resist: first, methacrylic acid/methyl methacrylate (MAA EL13) baked for 3 min at  $185^\circ\text{C}$  and second, poly(methyl methacrylate) (PMMA A3) baked for 30 min at  $185^\circ\text{C}$ . Once the  $e$ -beam patterning completed, we develop in an IPA:  $\text{H}_2\text{O}$  (3:1) bath at  $6^\circ\text{C}$  for 2 min, rinse for 10 s in IPA and blow dry. Finally, residual organic contaminants below the bridges are stripped by an  $\text{O}_2$  plasma for 10 s.

## 4. Junction deposition

The wafer is then introduced in an  $e$ -beam evaporator. We start with a 2-min argon-milling step at an angle of  $\pm 30^\circ$  to prepare for a good electrical contact with the Nb layer. We deposit two layers of aluminium (35 nm then 70 nm thick) at an angle of  $\pm 30^\circ$ , separated by a static oxidation in a pure  $\text{O}_2$  atmosphere at 10 mbar for 10 min. Before venting to air, the chamber is filled with 300 mbar of  $\text{O}_2$  for 5 min. We liftoff in a  $50^\circ\text{C}$  acetone bath for 1 h, transfer the wafer to a new acetone bath for 5 min and sonicate for 10 s, then rinse in IPA and blow dry. Images of the fabricated junctions are displayed in Fig. 5.

## APPENDIX B: CIRCUIT ANALYSIS

### 1. Asymmetrically threaded SQUID

The ATS is the nonlinear inductive dipole that mediates the exchange of pairs of photons between the memory and its environment. This dipole consists of a SQUID split in its center by an inductance at a specific dc flux bias and is represented by the circuit of Fig. 6.

The inductive energy of the ATS writes [11]

$$U_{\varphi_\Sigma, \varphi_\Delta}(\varphi) = \frac{1}{2} E_L \varphi^2 - 2E_J \cos(\varphi_\Sigma) \cos(\varphi + \varphi_\Delta) + 2\Delta E_J \sin(\varphi_\Sigma) \sin(\varphi + \varphi_\Delta), \quad (\text{B1})$$

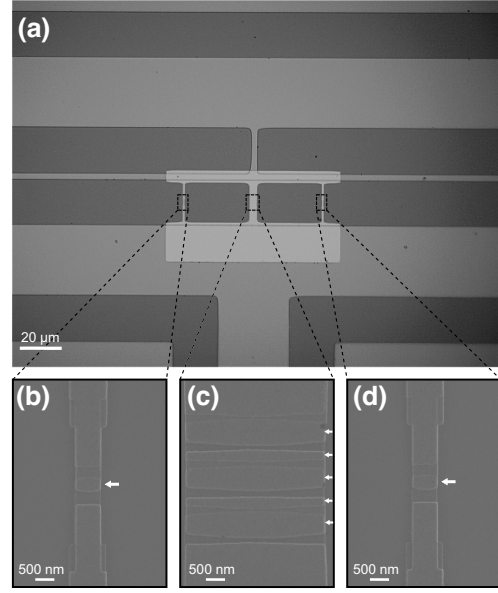


FIG. 5. (a) Optical micrograph of the ATS made of aluminium (light gray) deposited on the niobium circuit (gray) over a silicon substrate (dark gray). (b)–(d) Scanning electron microscope images of the small single junctions (b), (d) forming the SQUID loop and the five array junctions (c) forming the inductive shunt. The small junctions are  $275 \times 700 \text{ nm}^2$ . The array junctions, which would ideally all be equal in area, are in fact composed of three  $600 \text{ nm} \times 3.9 \mu\text{m}$  and two  $270 \text{ nm} \times 3.9 \mu\text{m}$  junctions. This results in a critical current density of about  $450 \text{ nA}/\mu\text{m}^2$ . For clarity, small arrows point to the location of each junction.

where  $E_L$  is the inductive energy of the shunt inductance,  $E_J \pm \Delta E_J$  are the Josephson energies of the left and right Josephson junctions, respectively,  $\varphi$  is the superconducting phase difference across the ATS and  $\varphi_{\Sigma, \Delta} = (\varphi_L \pm \varphi_R)/2$  are related to the common and differential flux threading the ATS with  $\varphi_{L,R}$  threading the left and right loop of the ATS, respectively.

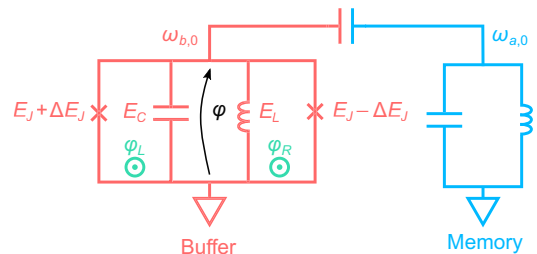


FIG. 6. Lumped-element model of the circuit. The buffer (red) with bare frequency  $\omega_{b,0}/2\pi$  is constituted with an ATS (inductive energy  $E_L$ , mean Josephson energy  $E_J$ , asymmetry  $\Delta E_J$ ), and a capacitor with charging energy  $E_C$ . The ATS loops are threaded with fluxes  $\varphi_L, \varphi_R$  (green) and is connected to the memory (blue), with bare frequency  $\omega_{a,0}/2\pi$ . The phase  $\varphi$  is indicated with an arrow (black).



## 2. Symmetries

The ATS potential has the following translational symmetries:

$$U_{\varphi_\Sigma, \varphi_\Delta}(\varphi) = U_{\varphi_\Sigma + \pi, \varphi_\Delta + \pi}(\varphi) = U_{\varphi_\Sigma + \pi, \varphi_\Delta - \pi}(\varphi), \quad (\text{B2})$$

and an inversion symmetry center at  $(\varphi_\Sigma, \varphi_\Delta) = (\pi/2, \pi/2)$ , such that

$$U_{\pi/2 + \varphi_\Sigma, \pi/2 + \varphi_\Delta}(\varphi) = U_{\pi/2 - \varphi_\Sigma, \pi/2 - \varphi_\Delta}(-\varphi). \quad (\text{B3})$$

Combining these three symmetries gives rise to a second inversion symmetry center located at  $(\varphi_\Sigma, \varphi_\Delta) = (\pi/2, -\pi/2)$ . Hence, all the information about the system is contained in the region  $\varphi_\Sigma \in [0, \pi]$ ,  $\varphi_\Delta \in [-\pi/2, \pi/2]$ . Note that provided  $\Delta E_J = 0$ , we have additional symmetry axes  $\varphi_\Sigma = 0$  and  $\varphi_\Delta = 0$ , such that

$$U_{\varphi_\Sigma, \varphi_\Delta}(\varphi) = U_{-\varphi_\Sigma, \varphi_\Delta}(\varphi) = U_{\varphi_\Sigma, -\varphi_\Delta}(-\varphi). \quad (\text{B4})$$

## 3. Saddle points

Let us study the potential around the inversion symmetry points  $(\varphi_\Sigma, \varphi_\Delta) = (\pi/2 + \epsilon, \pm\pi/2 + \delta)$

$$U(\varphi, \epsilon, \delta) = \frac{1}{2}E_L\varphi^2 \mp 2E_J \sin(\epsilon) \sin(\varphi + \delta) \pm 2\Delta E_J \cos(\epsilon) \cos(\varphi + \delta). \quad (\text{B5})$$

For small  $\epsilon$  and  $\delta$

$$U(\varphi, \epsilon, \delta) = \frac{1}{2}E_L\varphi^2 \mp (-2\Delta E_J + 2E_J\epsilon \mp \Delta E_J(\epsilon^2 + \delta^2)) \cos(\varphi) \mp (2E_J\epsilon + 2\Delta E_J\delta) \sin(\varphi). \quad (\text{B6})$$

For  $\epsilon = \delta = 0$ , the potential reaches its minimum at  $\varphi_{\min} = 0$ . At  $\epsilon, \delta \neq 0$ , we search for a first-order perturbation of  $\varphi_{\min}$ . Solving for  $(\partial/\partial\varphi)U(\varphi_{\min}, \epsilon, \delta) = 0$ , we get

$$\varphi_{\min} = \pm \frac{2E_J\epsilon + 2\Delta E_J\delta}{E_L \mp 2\Delta E_J}. \quad (\text{B7})$$

Around the minimum  $\varphi_{\min}$ , the second derivative of the potential with respect to  $\varphi$ , i.e., the inductive energy of the ATS writes

$$\frac{\partial^2}{\partial\varphi^2}U(\varphi_{\min}, \epsilon, \delta) = E_L \mp 2\Delta E_J + E_L\varphi_{\min}^2 \pm 2E_J\epsilon \mp \Delta E_J(\varphi_{\min}^2 - \epsilon^2 - \delta^2). \quad (\text{B8})$$

The ATS inductive energy has no linear terms in  $\epsilon$  or  $\delta$  so the points  $(\varphi_\Sigma, \varphi_\Delta) = (\pi/2, \pm\pi/2)$  are critical points of the inductive map of the ATS as a function of  $\epsilon$  and  $\delta$ .

Its quadratic dependence around the critical point has the following matrix representation:

$$M(E_L, E_J, \Delta E_J) = \frac{4(E_L \mp \Delta E_J)}{(E_L \mp 2\Delta E_J)^2} \begin{bmatrix} E_J^2 & E_J \Delta E_J \\ E_J \Delta E_J & \Delta E_J^2 \end{bmatrix} \pm \begin{bmatrix} \Delta E_J & E_J \\ E_J & \Delta E_J \end{bmatrix} \quad (\text{B9})$$

the determinant of which writes

$$\det(M) = E_L^2 \frac{\Delta E_J^2 - E_J^2}{(E_L \mp 2\Delta E_J)^2}. \quad (\text{B10})$$

The determinant is negative (provided  $\Delta E_J < E_J$ ) hence the critical point is a saddle point. This property is used to tune the dc working point experimentally (see Fig. 9). When  $\Delta E_J \neq 0$ , the two points  $(\varphi_\Sigma, \varphi_\Delta) = (\pi/2, \pm\pi/2)$  are nonequivalent saddle points of the ATS with inductive energy  $E_L \mp 2\Delta E_J$ .

## 4. Circuit Hamiltonian

The dynamics of the circuit displayed in Fig. 1 is well captured by a reduced lumped-element model (see Fig. 6) with the following Hamiltonian [11]:

$$H = \hbar\omega_{a,0}a^\dagger a + \hbar\omega_{b,0}b^\dagger b - 2E_J \cos(\varphi_\Sigma) \cos(\varphi + \varphi_\Delta) + 2\Delta E_J \sin(\varphi_\Sigma) \sin(\varphi + \varphi_\Delta), \quad (\text{B11})$$

where  $a, b$  are the memory and buffer annihilation operators. The buffer's angular frequency verifies  $\omega_{b,0} = \sqrt{8E_L E_C}/\hbar$ , where  $E_L, E_C$  are the energies associated to the buffer's inductive and capacitive shunt, respectively. The angular frequency of the memory is denoted  $\omega_{a,0}$ . We denote  $2E_J$  the sum of the Josephson energies of the single junctions composing the SQUID loop, and  $2\Delta E_J$  their difference. During fabrication we aim for the smallest possible junction asymmetry, however in practice we are left with  $\Delta E_J/E_J \approx 0.5\%$  (see Appendix C 1) which leads to spurious Kerr and cross-Kerr effects. We neglect  $\Delta E_J$  in the rest of the analysis. The ATS is threaded with a common and differential flux  $\varphi_{\Sigma, \Delta} = \frac{1}{2}(\varphi_L \pm \varphi_R)$ , where  $\varphi_{L,R}$  is the flux threading the left and right loop of the ATS. In the limit where the hybridization factor  $\nu$  between the buffer and memory is much smaller than 1, the phase across the ATS denoted  $\varphi$ , verifies  $\varphi = \varphi_b (b + b^\dagger + \nu(a + a^\dagger))$ , where the zero-point phase fluctuations for the buffer reads  $\varphi_b = (2E_C/E_L)^{1/4}$ .

### 5. First-order Hamiltonian at the operating point

By flux pumping the ATS around a well-chosen dc working point [11]

$$\begin{aligned}\varphi_\Sigma &= \frac{\pi}{2} + \epsilon_p \cos(\omega_p t), \\ \varphi_\Delta &= \frac{\pi}{2},\end{aligned}\quad (\text{B12})$$

we engineer a two-to-one photon exchange Hamiltonian between the memory and the buffer, provided the pump frequency  $\omega_p$  is close to the matching condition  $\omega_p = 2\omega_a - \omega_b$ . This two-to-one photon exchange Hamiltonian converts the strong single-photon losses of the buffer into an effective two-photon loss channel for the memory.

Likewise, a microwave drive at frequency  $\omega_d$  close to the buffer frequency, is converted into an effective two-photon drive of the memory (or squeezing) at frequency  $(\omega_d + \omega_p)/2$ . By definition, this frequency is close to the memory frequency.

For the memory, the combination of the two-photon loss and two-photon drive, stabilizes two coherent states with frequency  $(\omega_p + \omega_d)/2$  of equal amplitude and opposite phase. The heterodyne demodulation frequency  $\omega_{\text{dm}}$  for the memory is constrained accordingly

$$\omega_{\text{dm}} = \frac{\omega_p + \omega_d}{2}. \quad (\text{B13})$$

By going in the frame rotating at frequency  $\omega_{\text{dm}}$  for the memory and  $\omega_d$  for the buffer and performing first-order rotating-wave approximation (RWA), the Hamiltonian (B11) writes [11]

$$H/\hbar = -\Delta_a a^\dagger a - \Delta_b b^\dagger b + g_2^* a^2 b^\dagger + g_2 a^{\dagger 2} b, \quad (\text{B14})$$

where  $\Delta_a = \omega_{\text{dm}} - \omega_a$ ,  $\Delta_b = \omega_d - \omega_b$ , and  $\omega_a$  and  $\omega_b$  are, respectively, the memory and buffer frequency accounting for the ac-Stark shift due to the pump [11].

Incorporating the buffer drive and the dissipation of the two modes, the dynamics of the system is governed by

$$\begin{aligned}H/\hbar &= -\Delta_a a^\dagger a - \Delta_b b^\dagger b + g_2^* a^2 b^\dagger \\ &\quad + g_2 a^{\dagger 2} b - \epsilon_d b^\dagger - \epsilon_d^* b, \\ L_a &= \sqrt{\kappa_a} a, \\ L_b &= \sqrt{\kappa_b} b,\end{aligned}\quad (\text{B15})$$

where  $\epsilon_d$  is the buffer drive strength and  $\kappa_a$  and  $\kappa_b$  are the single-photon loss rate of the memory and the buffer, respectively.

We gain further insight on the dynamics of the system by performing the adiabatic elimination of the buffer. This is justified provided  $g_2 \ll \kappa_b$ . Following the method of Ref.

[30], we find that the reduced dynamics of the memory is given by

$$\begin{aligned}H_a/\hbar &= -\Delta_a a^\dagger a - \epsilon_d \gamma a^{\dagger 2} - \epsilon_d \gamma^* a^2 + \Delta_b |\gamma|^2 a^{\dagger 2} a^2, \\ L_{a2} &= \sqrt{\kappa_b |\gamma|^2} a^2, \\ L_a &= \sqrt{\kappa_a} a,\end{aligned}\quad (\text{B16})$$

with

$$\gamma = \frac{g_2}{\Delta_b + i\kappa_b/2}. \quad (\text{B17})$$

At  $\Delta_a = \Delta_b = 0$ , we recover Eq. (1)

$$\begin{aligned}H_2/\hbar &= i\epsilon_2 a^{\dagger 2} - i\epsilon_2^* a^2, \\ L_2 &= \sqrt{\kappa_2} a^2, \\ L_1 &= \sqrt{\kappa_a} a,\end{aligned}\quad (\text{B18})$$

with  $\epsilon_2 = 2\epsilon_d g_2/\kappa_b$  and  $\kappa_2 = 4|g_2|^2/\kappa_b$ .

### 6. Steady-state photon number

In this paragraph, we derive the stationary mean photon number in the memory using a semiclassical approximation

In the interaction picture, the dynamics arising from Eq. (B15) writes

$$\begin{aligned}\frac{da}{dt} &= \left(i\Delta_a - \frac{\kappa_a}{2}\right)a - 2ig_2 a^\dagger b, \\ \frac{db}{dt} &= \left(i\Delta_b - \frac{\kappa_b}{2}\right)b - ig_2^* a^2 + i\epsilon_d.\end{aligned}\quad (\text{B19})$$

We perform a mean-field approximation on modes  $a$  and  $b$ , and compute the steady-state of the simplified dynamics. The operators  $a$  and  $b$  are replaced by their mean value, the complex numbers  $\alpha$  and  $\beta$ .

This system always admits a solution in which the memory is in vacuum and corresponds to

$$\begin{aligned}\alpha &= 0, \\ \beta &= \frac{-\epsilon_d}{\Delta_b + i\kappa_b/2}.\end{aligned}\quad (\text{B20})$$

This solution is stable provided it is the only solution of Eq. (B19) for a given set parameters.

Assuming  $\alpha \neq 0$ , we can write

$$\begin{aligned}i\frac{\kappa_a}{2} + \Delta_a &= 2g_2\beta e^{-2i\theta_a}, \\ \left(i\frac{\kappa_b}{2} + \Delta_b\right)\beta &= g_2^* \alpha^2 - \epsilon_d,\end{aligned}\quad (\text{B21})$$

where  $\theta_a = \arg(\alpha)$ .

Solving for  $\beta$  in the first equation and injecting in the second one, we get

$$|\alpha|^2 = \frac{\epsilon_d}{g_2^*} e^{-2i\theta_a} + z, \quad (B22)$$

with  $z = \frac{(i\kappa_a/2 + \Delta_a)(i\kappa_b/2 + \Delta_b)}{2|g_2|^2}.$

### 7. Zero detuning

When  $\Delta_a = \Delta_b = 0$ , Eq. (B22) simplifies into

$$|\alpha|^2 = \frac{\epsilon_d}{g_2^*} e^{-2i\theta_a} - \frac{\kappa_a \kappa_b}{8|g_2|^2}, \quad (B23)$$

leading to

$$\begin{aligned} |\alpha|^2 &= \max \left[ \left| \frac{\epsilon_d}{g_2^*} \right| - \frac{\kappa_a \kappa_b}{8|g_2|^2}, 0 \right], \\ &= \max \left[ \left| \frac{\epsilon_d}{g_2^*} \right| \left( 1 - \frac{\kappa_a}{4|\epsilon_2|} \right), 0 \right]. \end{aligned} \quad (B24)$$

We recover the critical point when the two-photon drive overcomes the cavity dissipation.

In the absence of calibrated input or output lines, the power radiated by the memory is defined up to a constant, in particular, the quantity  $|g_2 \alpha|^2$  writes

$$|g_2 \alpha|^2 = \max \left[ |\epsilon_d g_2| - \frac{\kappa_a \kappa_b}{8}, 0 \right], \quad (B25)$$

which, as a function of  $\epsilon_d g_2$ , has a slope 1 and an  $x$  intercept  $\kappa_a \kappa_b / 8$ .

In terms of the single-mode effective quantities, Eq. (B24) rewrites for  $\epsilon_2 \geq \kappa_a / 4$

$$|\alpha|^2 = \frac{1}{2\kappa_2} (4\epsilon_2 - \kappa_a) \quad (\text{two-photon dissipation}).$$

If instead of two-photon dissipation, the Kerr effect of amplitude  $K$  limits the amplitude of the pointer states [31,32], a similar semiclassical analysis predicts a mean photon number for  $\epsilon_2 \geq \kappa_a / 4$

$$|\alpha|^2 = \frac{1}{2K} \sqrt{(4\epsilon_2)^2 - (\kappa_a)^2} \quad (\text{dissipative Kerr}),$$

which is qualitatively different from what is observed in this experiment.

### 8. General case

Since  $\theta_a$  and  $\alpha$  are on separate sides of Eq. (B22), we can geometrically solve the system in the complex plane. The right-hand side is a circle of radius  $|\epsilon_d / g_2^*|$  centered on  $z$ . The left-hand side is the positive real axis. In this picture, there can be 0, 1, or 2 intersections between this circle

and the real positive axis, giving rise to 1, 3, or 5 solutions for the system, one for vacuum plus two for each intersection since  $\pm\alpha$  are both valid solutions. Experimentally observed solutions are the ones that give rise to the largest field in the memory. Hence  $|\alpha|^2$ , the mean photon number in steady state, writes

$$|\alpha|^2 = \begin{cases} \max \left[ \text{Re}(z) + \sqrt{\left| \frac{\epsilon_d}{g_2^*} \right|^2 - \text{Im}(z)^2}, 0 \right], & \text{if } \left| \frac{\epsilon_d}{g_2^*} \right|^2 > \text{Im}(z)^2 \\ 0, & \text{otherwise.} \end{cases} \quad (B26)$$

In the  $\Delta_a, \Delta_b$  coordinates, the region where  $\alpha^2$  is nonzero forms a diamond shape. Hereafter, we provide the equation for the borders of this feature colloquially referred to as a diamond.

The  $\Delta_a, \Delta_b$  plane is divided into two domains depending on the sign of the quantity  $\Delta_a \Delta_b - \kappa_a \kappa_b / 4$ .

The top-right and bottom-left edges of the diamonds are located in the positive domain and given by

$$\kappa_a \Delta_b + \kappa_b \Delta_a = \pm 4 |\epsilon_d g_2|. \quad (B27)$$

Note that the slope of this edge is given by  $-\kappa_b / \kappa_a$ . The bottom-right and top-left edges are located in the negative domain and given by

$$\left( \frac{\kappa_a^2}{4} + \Delta_a^2 \right) \left( \frac{\kappa_b^2}{4} + \Delta_b^2 \right) = |2\epsilon_d g_2|^2. \quad (B28)$$

Hence the border of the diamond depends only on the product  $\epsilon_d g_2$  and does not carry information on  $g_2$  nor  $\epsilon_d$  independently. Moreover, we cannot determine  $g_2$  and  $\epsilon_d$  even with the full diamond information (not only the edges). Indeed, from the measurement of the rates  $\kappa_a, \kappa_b$  and the knowledge of the applied detunings  $\Delta_a, \Delta_b$ , one has independent access to the quantity

$$z' = \frac{1}{2} \left( i \frac{\kappa_a}{2} + \Delta_a \right) \left( i \frac{\kappa_b}{2} + \Delta_b \right). \quad (B29)$$

In the absence of photon-number calibration, we learn only from Eq. (B26) that the power radiated by the memory is proportional to

$$\langle I^2 \rangle \propto \text{Re}(z') + \sqrt{|\epsilon_d g_2|^2 - \text{Im}(z')^2}. \quad (B30)$$

Thus, we have access only to the product  $\epsilon_d g_2$  but not  $g_2$  or  $\epsilon_d$  independently.

## APPENDIX C: TUNING THE EXPERIMENT

Our experiment requires dc and rf powering. For optimal operation, two dc currents and two rf powers and frequencies need to be fine tuned. In this section we describe the sequence of calibration experiments we perform to set the working point.

### 1. dc currents

The first calibration experiment we perform is to extract the buffer and memory frequencies as a function of the common and differential flux in the ATS loop (see Fig. 7). From these maps we identify the circuit parameters and locate the ATS saddle points.

In the following, we describe the measurement protocol to acquire the buffer frequency flux map. We set a tone at frequency  $f$  on the buffer port and record its reflected amplitude and phase as a function of the dc voltages  $V_{\Sigma,\Delta} = (V_L \pm V_R)/2$  (see Fig. 8). The physical controls  $V_{\Sigma,\Delta}$  are transformed to the common and differential flux basis  $\varphi_{\Sigma,\Delta}$  to match the symmetries of the circuit Hamiltonian (B11). A variation in the reflected signal is detected at flux points  $\varphi_{\Sigma,\Delta}(f)$  where the buffer frequency enters the vicinity of  $f$ . This sequence is repeated by scanning  $f$  in between 5.2 and 9 GHz in steps of 100 MHz. In Fig. 7, the frequency  $f$  is encoded in the color of pixels located at  $\varphi_{\Sigma,\Delta}(f)$ . We repeat the same protocol on the memory port to extract the memory frequency flux map.

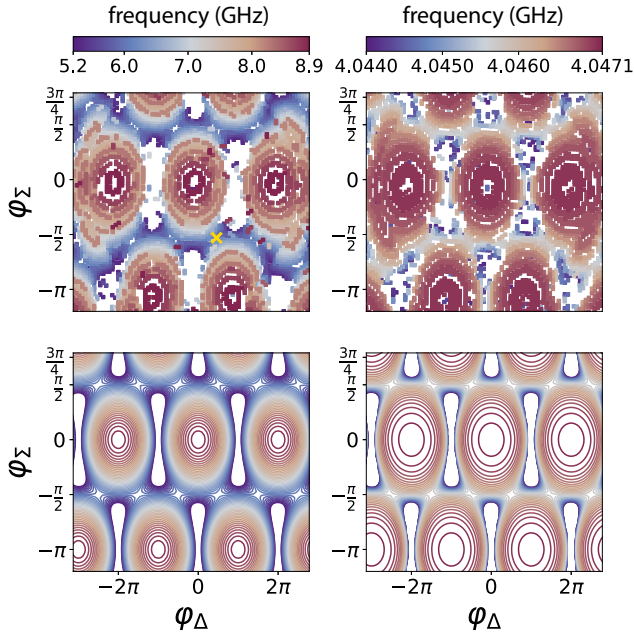


FIG. 7. Measured (top) and simulated (bottom) frequencies (color) of the buffer (left) and memory (right) as a function of the differential flux ( $x$  axis) and common flux ( $y$  axis) in the ATS loop. The orange cross marks the flux point at which we operate the experiment.

The theory plots in Fig. 7 are obtained for the numerical diagonalization of the Hamiltonian in Eq. (B11). From the ATS symmetries, we know that there exist two nonequivalent families of saddle points, those generated from  $(\varphi_\Delta, \varphi_\Sigma) = (-\pi/2, \pi/2)$ , and those from  $(\varphi_\Delta, \varphi_\Sigma) = (\pi/2, \pi/2)$ . The junction asymmetry  $\Delta E_J$  lifts the degeneracy of the buffer frequency between these points.

We refine the flux and frequency sweeps around these saddle points in order to precisely pin down their location. In Fig. 9, we directly display the reflected amplitude on the buffer port at different frequencies  $f$ . A saddle point is easily identified as the closing of the buffer frequency contour line. Note that the saddle point at  $(-\pi/2, \pi/2)$  appears at  $f_{b1} = 6.00$  GHz as shown in the top middle panel. The second one appears at  $f_{b2} = 6.04$  GHz as shown in the bottom middle panel.

The parameters entering Eq. (B11) are listed in Table I. The charging energy  $E_C$  is extracted from three-dimensional finite elements' electromagnetic simulations. The inductive energy  $E_L$  and the junction asymmetry  $\Delta E_J$  are computed from the buffer frequencies at the saddle points that verify, in the weakly hybridized limit:

$$f_{b1,b2} = \frac{1}{h} \sqrt{8E_C(E_L \pm 2\Delta E_J)}.$$

The Josephson energy  $E_J$  is extracted from the maximum buffer frequency  $f_{b\max}$  measured in the buffer flux map of Fig. 7. This maximum value  $f_{b\max} = 8.9$  GHz is reached for  $(\varphi_\Delta, \varphi_\Sigma) = (0, 0)$  and verifies, in the weakly hybridized limit:  $f_{b\max} = (1/h)\sqrt{8E_C(E_L + 2E_J)}$ .

The memory frequency  $f_a$  is extracted from the memory frequency flux map in Fig. 7 at the saddle points. Due to the weak hybridization with the buffer, the memory frequency difference at the two saddle points is negligible. Finally we numerically find the hybridization factor  $\nu$  that produces a memory frequency flux map in agreement with the data in Fig. 7.

### 2. Phase locking

In the laboratory frame, at any point in time, the phase of the pointer states resulting from the junction mixing process is given by

$$\theta_a = (\theta_p + \theta_d)/2, \quad (C1)$$

where  $\theta_p$  and  $\theta_d$  are, respectively, the pump and drive tone phase. The pump tone is directly generated by the microwave signal generator and pulsed via a microwave switch whereas the drive tone is pulsed via an  $IQ$  mixer (Fig. 8). The resulting phases of the tones are

$$\theta_p = \theta_p^{\text{LO}}, \quad \theta_d = \theta_d^{\text{LO}} + \theta_d^{\text{IF}}, \quad (C2)$$



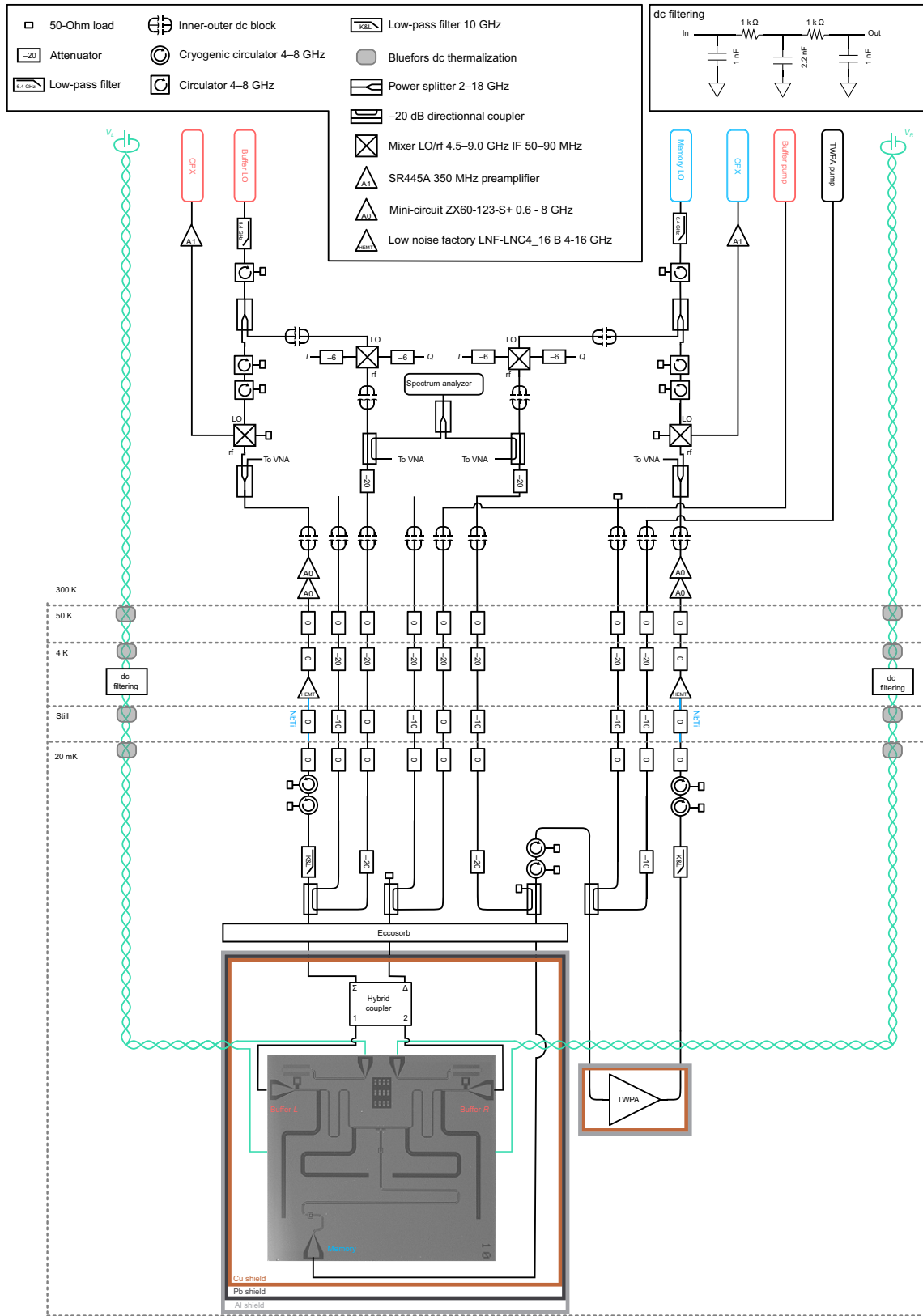


FIG. 8. Wiring of the experiment. Measurement apparatus for the memory (blue labels), buffer (red labels), and TWPA pump (black label) connect to the experiment through rf lines (black lines). dc voltage sources are used to drive flux lines (green lines). Dashed lines indicate the different temperature stages of the dilution refrigerator. Additional information is provided in the legend (gray background), annotations and in the text.

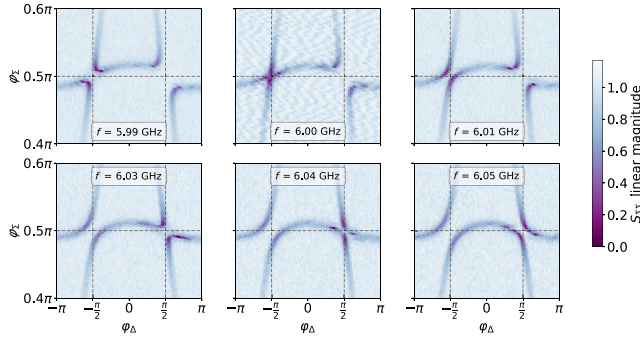


FIG. 9. Each panel displays the measured relative amplitude (color) of the reflected signal on the buffer port at the frequency  $f$  specified in each label box, as a function of the differential ( $x$  axis) and common ( $y$  axis) phase biases. The dashed gray lines are guides for the eye corresponding to  $\varphi_\Delta = \pm\pi/2$  and  $\varphi_\Sigma = \pi/2$ .

where  $\theta_p^{\text{LO}}$  and  $\theta_d^{\text{LO}}$  are the local oscillator (LO) phases of the microwave generator and  $\theta_d^{\text{IF}}$  is the intermediate frequency (IF) signal phase delivered by the arbitrary waveform generator (AWG) channel to pulse the drive tone. The radiated signal from the memory is demodulated in a frame with phase

$$\theta_{\text{dm}} = \theta_{\text{dm}}^{\text{LO}} + \theta_{\text{dm}}^{\text{IF}}, \quad (\text{C3})$$

where  $\theta_{\text{dm}}^{\text{LO}}$  is the phase of the demodulation LO and  $\theta_{\text{dm}}^{\text{IF}}$  is the phase of the analog-digital converter (ADC). In order to phase lock the pointer states with the demodulation frame, we should ensure

$$\theta_a - \theta_{\text{dm}} = \text{constant}. \quad (\text{C4})$$

The three LOs are generated with a single four-channel Anapico signal generators, and the two IFs with a single Quantum Machines OPX. The accuracy of these instruments ensures that all the LOs share the same time reference and all the IFs share the same time reference.

TABLE I. Buffer and memory parameters entering the Hamiltonian (B11).  $E_C$  and  $E_I$  are, respectively, the buffer's charging and inductive energy.  $E_J$  and  $\Delta E_J$  are the ATS mean Josephson energy and asymmetry.  $\omega_{b,0}/2\pi$  and  $\omega_{a,0}/2\pi$  are buffer and memory bear frequencies.  $\varphi_b$  is the buffer zero-point fluctuations.  $\nu$  is the hybridization strength. From these numbers, we can estimate the Kerr nonlinearity of the memory  $K_a < 1$  Hz.

$E_C/h$	72.6 MHz
$E_I/h$	62.40 GHz
$E_J/h$	37.00 GHz
$\Delta E_J/h$	0.207 GHz
$\omega_{b,0}/2\pi$	6.020 GHz
$\varphi_b$	0.220
$\omega_{a,0}/2\pi$	4.0457 GHz
$\nu$	3.6%

However, given the high frequencies at stake, the instrument sharing the same 50-MHz clock is not sufficient for this two-time reference to be considered identical. The LO time is referred to as  $t$  and the IF time as  $t'$ . Hence,

$$\begin{aligned} \theta_a - \theta_{\text{dm}} &= (\omega_p^{\text{LO}} t + \omega_d^{\text{LO}} t + \omega_d^{\text{IF}} t')/2 \\ &\quad + \text{constant} - (\omega_{\text{dm}}^{\text{LO}} t + \omega_{\text{dm}}^{\text{IF}} t') + \text{constant}, \\ &= ((\omega_p^{\text{LO}} + \omega_d^{\text{LO}})/2 - \omega_{\text{dm}}^{\text{LO}})t + (\omega_d^{\text{IF}}/2 - \omega_{\text{dm}}^{\text{IF}})t', \end{aligned} \quad (\text{C5})$$

and the phase-locking condition imposes the frequency-matching conditions

$$\begin{aligned} (\omega_p^{\text{LO}} + \omega_d^{\text{LO}})/2 - \omega_{\text{dm}}^{\text{LO}} &= 0, \\ \omega_d^{\text{IF}}/2 - \omega_{\text{dm}}^{\text{IF}} &= 0. \end{aligned} \quad (\text{C6})$$

### 3. Pump and drive frequencies

Once the dc biases are tuned at one saddle point and the memory and buffer resonance frequencies are determined by direct spectroscopy in reflection on their respective ports, we proceed to tune the pump and drive tones. The pump frequency is determined via two-tone spectroscopy: a weak drive tone is used to perform buffer spectroscopy while sweeping the pump frequency around the frequency-matching condition  $\omega_p = 2\omega_a - \omega_b$ . As this operation is being performed, we also perform the heterodyne detection of the field radiated by the memory (Fig. 10).

When the two-to-one photon exchange is resonant, a sharp feature is observed within buffer resonance, referred to as a diamond, and the memory starts to radiate power. The discrepancy between the ideal and measured diamond shape is used as a witness for the appearance of higher-order processes. The pump amplitude is set so as to maximize  $g_2$  while mitigating detrimental higher-order effects.

In order to minimize the amount of data collected and accurately enlarge the diamond feature, Fig. 10(a) is acquired in the following way:

- at a fixed pump frequency ( $x$  axis of Fig. 10) the buffer spectroscopy is done by varying the buffer IF frequency with a fixed LO frequency. Due to the frequency constraint of Eq. (C6) the heterodyne detection of the radiated memory field is done by varying the memory IF frequency with a fixed LO frequency.
- for the demodulation frequency to remain close to the memory frequency while varying the pump frequency, ( $y$  axis of Fig. 10) the pump and drive LO frequencies are varied in opposite directions. In this way, we have  $\omega_p + \omega_b^{\text{LO}} = 2\omega_{\text{dm}}^{\text{LO}} = \text{constant}$ .

In these coordinates,  $\Delta_b$  and  $2\Delta_a$  are varied along the  $x$  axis and  $\Delta_b$  is varied along the  $y$  axis. If there is no Stark

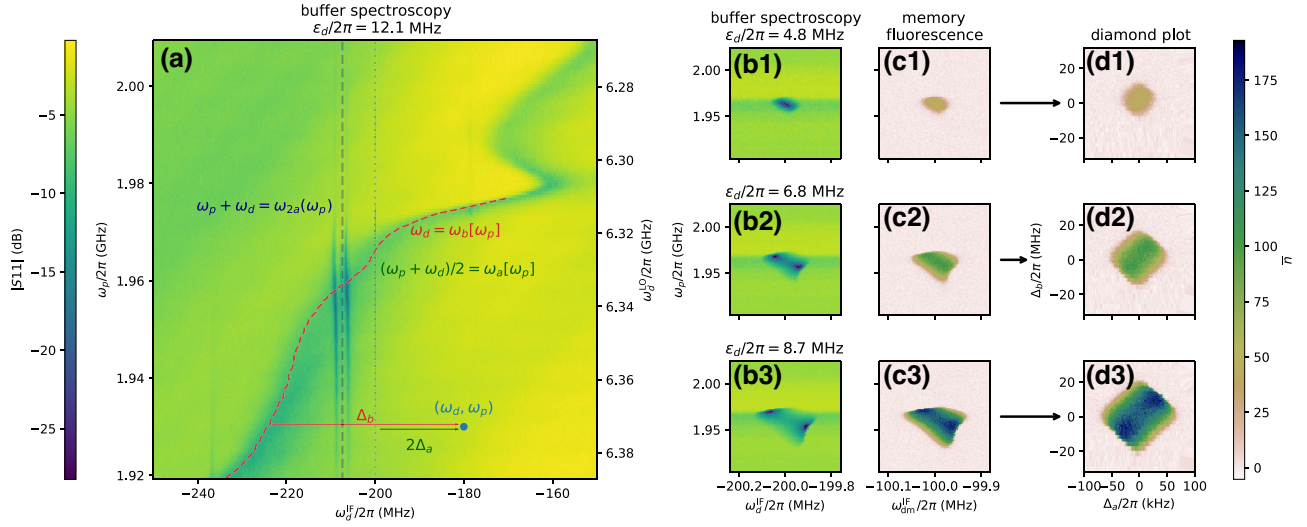


FIG. 10. (a) Relative amplitude (color) of the reflected signal on the buffer port as a function of the pump frequency  $\omega_p$  (left y axis), drive local oscillator frequency  $\omega_d^{\text{LO}}$  (right y axis) and drive intermediate frequency  $\omega_d^{\text{IF}}$  (x axis). The drive frequency is given by  $\omega_d = \omega_d^{\text{IF}} + \omega_d^{\text{LO}}$ . For each pump frequency, the drive LO frequency is set to  $\omega_d^{\text{LO}} = (2\omega_a - \omega_p) + 200$  MHz, such that vertical lines correspond to constant detuning from the frequency-matching condition ( $\Delta_a = cte$ ). The buffer drive resonance condition  $\Delta_b = 0$  is determined by fitting each horizontal cuts of the map (dashed red line). In the vicinity of  $\Delta_a = 0$  and  $\Delta_b = 0$ , a sharp feature indicates that the two-to-one photon exchange transition is resonant (dotted green line). Spurious transitions appear near the frequency-matching condition  $\omega_p + \omega_d = \omega_{2a}$  (blue dashed line), where  $\omega_{2a}$  is the frequency of the second harmonic of the memory  $\lambda/2$ -resonator measured independently. (b) Enlargement of the two-to-one photons' exchange transition for increasing drive amplitude  $\epsilon_d$ . (c) Radiated energy from the memory in units of circulating photon number (color) as a function of the pump frequency  $\omega_p$  (left y axis) and two-photon drive intermediate frequency  $\omega_{\text{dm}}^{\text{IF}}$  (x axis), for increasing drive amplitude. On these panels, the two-photon drive LO frequency is set to  $\omega_{\text{dm}}^{\text{LO}} = \omega_a + 100$  MHz. When the two-to-one photon exchange transition is resonant, the engineered two-photon drive populates the memory. The average occupation of the memory is determined thanks to an undercoupled port via heterodyne detection. (d) Radiated energy from the memory in units of circulating photon number (color) as a function of the pump and drive detuning from the frequency-matching condition  $\Delta_a$  (x axis), and the drive detuning from the buffer  $\Delta_b$  (y axis). In these coordinates, the feature takes the shape of a regular diamond.

shift, the buffer resonance would be a diagonal line of slope 1 and the memory line (when the two-photon drive is tuned with the memory mode) a vertical line. In practice, these two lines are distorted and we numerically fit the buffer and memory frequencies as a function of the pump frequency to perform the change of basis leading to the diamond of Fig. 10(d) in the  $\Delta_a, \Delta_b$  coordinate system.

To perform this change of coordinates, we evaluate the following functions from measurements by linear interpolation:

$$\begin{aligned}\Delta_b &= f(\omega_d^{\text{IF}}, \omega_p) = \omega_d^{\text{IF}} + \omega_d^{\text{LO}} - \omega_b[\omega_p], \\ \Delta_a &= g(\omega_d^{\text{IF}}, \omega_p) = \frac{\omega_b^{\text{IF}}}{2} + \frac{\omega_p + \omega_d^{\text{LO}}}{2} - \omega_a[\omega_p], \quad (\text{C7}) \\ &= \omega_{\text{dm}}^{\text{IF}} + \omega_{\text{dm}}^{\text{LO}} - \omega_a[\omega_p].\end{aligned}$$

For each data point, we can now compute the actual value of  $\Delta_a$  and  $\Delta_b$ . This enables us to display radiated energy by the memory in the basis of Hamiltonian Eq. (B15): previously distorted, the diamonds recover their shape.

By construction, diamond center should coincide with the zero detuning point. By exploiting the diamonds' inversion symmetry, we can verify that the maximum of the auto-correlation function

$$\begin{aligned}(\Delta_a^0, \Delta_b^0) &= \\ \max_{(\Delta_a, \Delta_b)} &\left( \iint |\alpha|^2(\delta_a, \delta_b) |\alpha|^2(\Delta_a - \delta_a, \Delta_b - \delta_b) \delta_a \delta_b \right) \quad (\text{C8})\end{aligned}$$

gives back the zero detuning point, up to a slight discrepancy due to the diamond imperfection. Experimentally, we find the zero detuning point as the convergence point of the diamond feature at vanishingly small drive amplitude [see Fig. 10(c)]. All three centers (construction, autocorrelation, experimental) are shown in Fig. 11 and lie in a small region at the center of the diamond. The system parameters at the operating point are summarized in Table II.

#### APPENDIX D: PHOTON-NUMBER CALIBRATION

It is of central importance that our macroscopic bit-flip times are observed for states containing only a few tens of

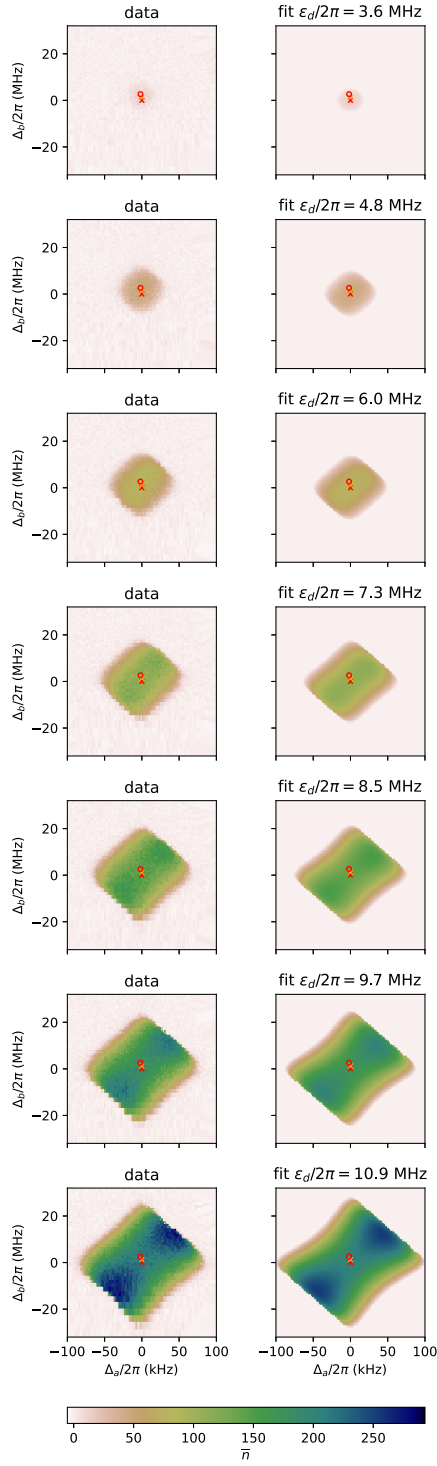


FIG. 11. Radiated energy from the memory in units of circulating photon number (color) as a function of the detuning from the frequency matching condition  $\Delta_a$  (x axis), and the detuning from the buffer resonance  $\Delta_b$  (y axis). Left column displays data, right column displays semiclassical simulations for the corresponding drive amplitude. Orange cross shows the position of the maximum of the autocorrelation for the largest drive amplitude. Red cross shows the zero detuning point given by direct fit of memory and buffer spectroscopy. Red circle is the point at which well-averaged data are taken to perform the fit of  $g_2$ .

TABLE II. Parameters at the operating point of the experiment.  $\omega_b/2\pi$ ,  $\omega_a/2\pi$ ,  $\omega_p/2\pi$  are the buffer, memory, and pump frequencies.  $\kappa_a^i$ ,  $\kappa_a^c$  are the internal and coupling loss rates of the memory,  $\kappa_b$  is the loss rate of the buffer,  $g_2$  is the two-photon coupling rate,  $\kappa_2/2\pi$  is the two-photon dissipation rate and  $\bar{n}_{\text{sat}}$  is the average number of photons at the bit-flip time saturation. The following parameters are given with confidence intervals:  $\kappa_a^i \in [15, 22]$  kHz,  $\kappa_a^c \in [39, 42]$  kHz,  $\kappa_b \in [13, 20]$  MHz,  $g_2/2\pi \in [30, 46]$  MHz,  $\kappa_2 \in [270, 410]$ ,  $\bar{n}_{\text{sat}} \in [43, 54]$ . The corresponding total quality factors are about 400 for the buffer, and 70 000 for the memory.

$\omega_b/2\pi$	6.1273 GHz	$\kappa_a^i/2\pi$	18 kHz	$g_2/2\pi$	39 kHz
$\omega_a/2\pi$	4.0458 GHz	$\kappa_a^c/2\pi$	40 kHz	$\kappa_2/2\pi$	370 Hz
$\omega_p/2\pi$	2.07 GHz	$\kappa_b/2\pi$	16 MHz	$\bar{n}_{\text{sat}}$	43

photons. Indeed it is only in the low photon-number regime that this system can operate as a coherent qubit. A reliable calibration of the number of photons  $\bar{n}$  is therefore key to this work. In this section, we describe two calibration methods, and check their consistency. We start by computing the mapping between the cavity-field properties and the measured quadratures. Then, we detail the method used in the main text to calibrate  $\bar{n}$  from the curvature at the critical point. Finally, we describe a method relying on the measurement of the detection efficiency  $\eta$ .

### 1. Heterodyne detection

The heterodyne detection of the field radiated by the memory results in two signals that are integrated over an integration time  $T_m$  to give out  $(I, Q)$  pairs of time traces

$$I_t = \sqrt{G} \int_t^{t+T_m} \left( \sqrt{2\kappa_a^c \eta} \text{Tr}(\rho_{t'}(a + a^\dagger)/2) dt' + dW_I \right),$$

$$Q_t = \sqrt{G} \int_t^{t+T_m} \left( \sqrt{2\kappa_a^c \eta} \text{Tr}(\rho_{t'}(a - a^\dagger)/2i) dt' + dW_Q \right),$$
(D1)

where  $G$  is the gain of the amplification chain,  $\kappa_a^c$  is the coupling rate of the memory,  $\eta$  is the quantum detection efficiency,  $\rho_t$  is the instantaneous state and  $dW_I$ ,  $dW_Q$  are the noises added to each quadrature that verify  $dW_I^2 = dW_Q^2 = dt$ . The statistics of the distribution of the  $(I, Q)$  pairs collected over time gives information about the memory state. In particular, we can verify that in the general case [33,34] and in the limit of small  $T_m$

$$\overline{I^2 + Q^2} = 2GT_m + 2G\kappa_a^c \eta T_m^2 \text{Tr}(\rho_\infty a^\dagger a),$$

$$= 2GT_m + 2G\kappa_a^c \eta T_m^2 \bar{n},$$
(D2)

where  $\bar{n}$  is the mean photon number,  $\overline{I^2 + Q^2}$  is the statistical average over the  $(I, Q)$  pairs collected over time and  $\rho_\infty$  is the steady-state density operator of the cavity. In our specific case, we verify both numerically and experimentally that this limit is practically reached for  $T_m = 10 \mu\text{s}$ .



In Eq. (D2), the offset  $GT_m$  can be calibrated out from the average of  $I^2 + Q^2$  when the cavity is in vacuum, which results in the average energy radiated by the cavity over a period  $T_m$  of

$$\overline{I^2 + Q^2} - \overline{I^2 + Q^2}\Big|_{\text{vac}} = 2G\kappa_a^c\eta T_m^2\bar{n}. \quad (\text{D3})$$

## 2. Critical point

For various values of buffer drive amplitude  $\epsilon_d$ , we measure the average energy radiated by the memory for a duration  $T_m = 10 \mu\text{s}$  according to Eq. (D2) (see Fig. 12), which is proportional to  $\bar{n}$ . The following paragraphs aim

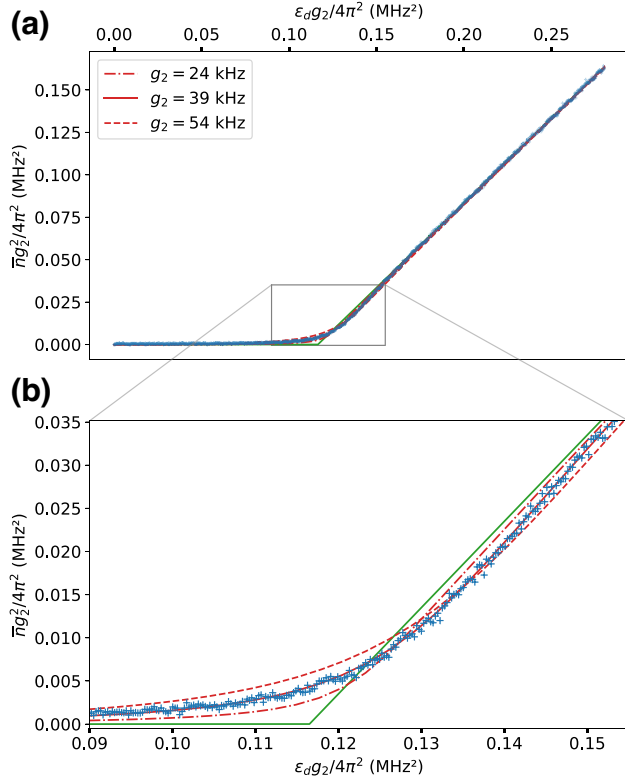


FIG. 12. Two-photon coupling calibration. (a) Radiated energy from the memory ( $y$  axis) as a function of drive amplitude ( $x$  axis). There are two regimes: when the drive amplitude is small, single-photon loss overcomes the two-photon drive, and the memory stays in the vacuum. Passed the critical point, the memory gets populated by a coherent state with photon number asymptotically proportional to the drive amplitude. The axes units are chosen so that the critical point is at  $\kappa_a\kappa_b/8$  and the asymptotic slope is 1. The data correspond to an integration time of  $10 \mu\text{s}$  with 10 000 averages (crosses). The semiclassical model (green solid line) captures the position of the critical point but fails to explain the curvature of the experimental data. A full numerical simulation is used to reproduce the data where the only fitting parameter is  $g_2$  (red lines). (b) Enlargement of the curvature around the critical point [gray rectangle from (a)], emphasizing the agreement between simulations and experimental data.

at calibrating this proportionality constant. First, we calibrate the axes such that the only unknown parameter is  $g_2$  using the semiclassical analysis. Then, we use the quantum fluctuation at the critical point to determine  $g_2$ . Finally, we explain how we use this calibration to estimate the memory photon number in a given trajectory.

## 3. Semiclassical

As shown by Eq. (B24) in the semiclassical approximation, at zero detuning, the critical point appears when  $|\epsilon_d g_2| = \kappa_a \kappa_b / 8$  and from there the mean photon number in the memory increases linearly with the drive amplitude. Using these properties, we calibrate the drive amplitude axis in units of  $|\epsilon_d g_2|$ : the  $x$  intercept of the linear dependence at large photon number (semiclassical regime) is located at  $\kappa_a \kappa_b / 8$ . The  $x$  axis being calibrated, we linearly stretch the  $y$  axis such that the asymptotic slope is 1 in the strong drive regime. According to Eq. (B25), this transformation enforces the  $y$  axis to  $|\alpha g_2|^2$  and leads to the scaled data of Fig. 12.

This rescaling crucially depends on the values of  $\kappa_a$  and  $\kappa_b$ , which are determined as follows. We measure the reflection coefficient of the memory in the presence of a pump tone slightly detuned from the frequency-matching condition. This enables to capture the shift of parameters (frequency, internal losses, coupling losses) due to non-linear effects arising from the pump while disabling the two-photon losses. From this measurement we numerically fit  $\kappa_a^i/2\pi \in [15, 22] \text{ kHz}$  and  $\kappa_a^c/2\pi \in [39, 42] \text{ kHz}$ . The same protocol fails to determine precisely  $\kappa_b$  due to the background induced by the band-stop filters and the strong dependence of the buffer parameters on the pump frequency. Instead, we use the diamond property derived in Eq. (B27) that the top-right and bottom-left edge of the diamond have a slope of  $-\kappa_b/\kappa_a$ . We find  $\kappa_b/2\pi$  in the range  $[13, 20] \text{ MHz}$  (Fig. 13).

We later propagate the parameter range found for  $\kappa_a$  and  $\kappa_b$  on the rest of the calibration to give a robust confidence interval for  $g_2$  and  $\bar{n}$ .

We can independently check the calibration of  $|\alpha g_2|^2$  by studying the excess internal losses arising from the two-photon dissipation. When the two-photon dissipation becomes resonant, the internal losses of the memory measured by direct spectroscopy increase drastically and become nonlinear as a function of the probe power. The effective internal losses of the memory write

$$\kappa_{a,\text{eff}}^i = \kappa_a^i + 2\kappa_2|\alpha|^2, \quad (\text{D4})$$

where  $\kappa_a^i$  is the bare internal losses of the cavity and  $|\alpha|^2$  is the average circulating photon number due to the spectroscopy tone. The excess losses rewrite  $8|\alpha g_2|^2/\kappa_b$  and provides an independent calibration of  $|\alpha g_2|^2$  that we find in good agreement with the previous method.

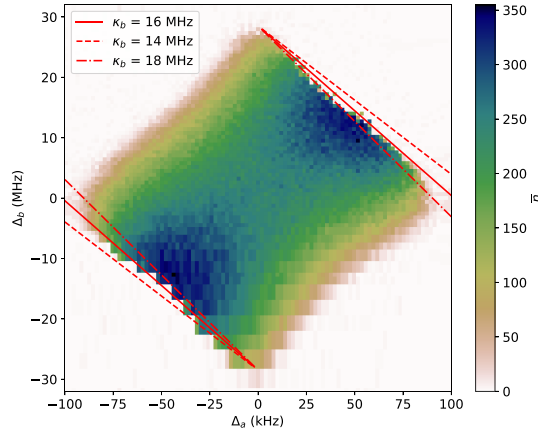


FIG. 13. Radiated energy from the memory in units of circulating photon number (color) as a function of the detunings  $\Delta_a$  ( $x$  axis), and  $\Delta_b$  ( $y$  axis) defined in the text, for the drive amplitude  $\epsilon_d/2\pi = 12.1$  MHz. The red solid line displays the fitted slope of the top-right and bottom-left edge, yielding the ratio  $\kappa_b/\kappa_a$  [see (B27)]. The red dashed-dotted lines and red dashed lines, respectively, give the upper and lower bound on this parameter (determined by graphical reading).

#### 4. Quantum signature

At the critical point, the semiclassical analysis fails to capture the curvature of the mean photon number  $\bar{n}$  as a function of the drive amplitude  $\epsilon_d$  (Fig. 2). This curvature results from the quantum fluctuations at the dissipative phase transition [22]. Instead, we perform a quantum analysis and compute the average photon number in the steady state  $\rho_\infty$  of the Lindblad equation generated by Eq. (B16),  $\bar{n} = \text{Tr}(\rho_\infty a^\dagger a)$  using the steadystate function imported from the QuTiP python package. Once we express  $|\alpha g_2|^2$  as a function of  $|\epsilon_d g_2|$  (see Fig. 12) the only fitting parameter is  $g_2$ . Given the range of  $\kappa_a$  and  $\kappa_b$ , we estimate  $g_2/2\pi \in [30, 46]$  kHz.

#### 5. Trajectory calibration

We analyze the bit-flip time scale over several orders of magnitude, hence we increase the integration time  $T_m$  to keep a manageable amount of data in long bit-flip traces. Thanks to the previous calibration, we can readily get the memory photon number from the  $(I, Q)$  statistics of the trace. Indeed, from Eq. (D2), we have both  $G$  from the value of  $\overline{I^2 + Q^2}|_{\text{vac}}$  and  $2G\kappa_a^c\eta$  from the calibration of  $\bar{n}$ . When given a trace with different integration time  $T'_m$ , we determine

$$\bar{n} = \frac{\overline{I^2 + Q^2} - 2GT'_m}{2G\kappa_a^c\eta T_m^2}. \quad (\text{D5})$$

#### 6. Quantum detection efficiency

A different route leading to  $\bar{n}$  is to measure the detection efficiency  $\eta$ . Indeed, for a coherent state containing a number of photons  $\bar{n}$ , the measured mean  $\bar{I}$ , and standard deviation  $\sigma(I)$  of the  $I$  quadrature verify

$$\bar{n} = \left( \frac{\bar{I}}{\sigma(I)} \right)^2 \frac{1}{2\eta\kappa_a^c T_m}. \quad (\text{D6})$$

Inversely, from the calibration of  $\bar{n}$  from the previous section, we estimate  $\eta \simeq 3\%$ .

In this section, we independently evaluate  $\eta$  by fabricating a device containing a memory mode coupled to a transmon that serves as an *in situ* measurement of  $\bar{n}$ .

The fabricated memory mode is identical to the one described in the main text, and the entire two-photon exchange apparatus is replaced with a transmon qubit (see Fig. 14). The chip is mounted in a similar sample holder and measured with an identical wiring as the experiment described in the main text. The characteristics of the chip are listed in Table III.

Our evaluation of  $\eta$  follows three steps. First, we perform a standard spectroscopy in reflection of the memory mode in order to emulate a measurement signal that is directly proportional to the intracavity field amplitude  $\langle a \rangle$ . Second, for a given amplitude  $a_{\text{in}}$ , we calibrate the cavity photon number  $\bar{n} = \langle a^\dagger a \rangle$  by resolving the photon-number splitting of the qubit. Third, for each calibrated photon

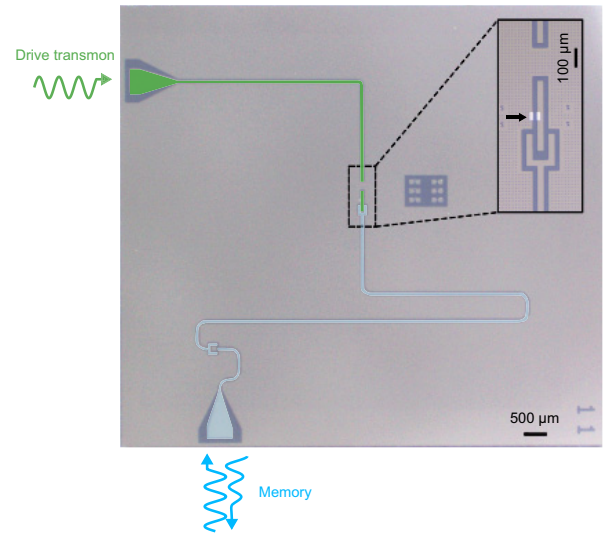


FIG. 14. False-color optical micrograph of the detection efficiency chip in Nb (gray) on Si (dark blue). The memory resonator (blue) is capacitively coupled to a transmon (green). The inset is centered on the transmon and its Josephson junction in Al (light gray). We can address the memory and collect the reflected signal (blue waves) via the bottom 50Ω port. The left 50Ω port is dedicated to drive the transmon (green waves). This sample is also used to measure the memory thermal population of about 1%.

TABLE III. Parameters of the device used to calibrate the quantum detection efficiency  $\eta$ . The transmon qubit lifetime and coherence times are denoted  $T_1$  and  $T_2$ . The memory coupling and internal loss rates are denoted  $\kappa_a^c$  and  $\kappa_a^i$ , and  $\chi$  corresponds to the dispersive coupling rate between the transmon and the memory.

$T_1$	19.3 $\mu$ s
$T_2$	24.3 $\mu$ s
$\kappa_a^c/2\pi$	38 kHz
$\kappa_a^i/2\pi$	17 kHz
$\chi/2\pi$	1.75 MHz

number we measure the fluctuations of the outgoing field  $a_{\text{out}}$  and retrieve  $\eta$  by inverting Eq. (D6). We detail each step of this procedure below.

### 7. Memory spectroscopy

For various incoming signal amplitudes  $S_{\text{in}}$ , we perform a spectroscopy measurement recording the reflected signal  $S_{\text{out}}$ . Using the results of the resonance fit, we can then translate the data in the  $(I, Q)$  plane in order to emulate a transmission signal:  $S_t = A \langle a \rangle$ , where  $A$  is an unknown scaling factor to be calibrated.

### 8. Photon-number-resolved qubit spectroscopy

For various resonant signal amplitudes  $S_{\text{in}}$  we activate a drive on the transmon at a fixed amplitude  $S_q$  with a varying detuning  $\Delta_q$ . The data  $S_t(\Delta_q, S_{\text{in}}, S_q)$  are then fitted to the result of a numerical simulation that we detail in the following. Using the `steadystate` function of the QuTiP package [35,36], we solve the following dynamics:

$$\begin{aligned} \partial_t \rho &= -i[H, \rho] + D[\sqrt{\kappa_a}a]\rho + D[\sqrt{\kappa_i}q]\rho \\ &\quad + D[\sqrt{\kappa_\phi}q^\dagger q]\rho, \\ H &= \Delta_q q^\dagger q - \chi a^\dagger a q^\dagger q + \Omega_a (a + a^\dagger) + \Omega_q (q + q^\dagger), \end{aligned}$$

where  $a$  (respectively,  $q$ ) is the memory (respectively, qubit) mode annihilation operator,  $\kappa_1 = 1/T_1$ ,  $\kappa_\phi = (1/T_2) - (1/2T_1)$ ,  $\Omega_a$  (respectively,  $\Omega_q$ ) is the drive on the memory (respectively, qubit) and the remaining parameters are defined in Table III. From this simulation we extract  $\langle a \rangle$  ( $\Delta_q, \Omega_a, \Omega_q$ ), that is used to fit the dataset  $S_t(\Delta_q, S_{\text{in}}, S_q)$ , where the fit parameters are the proportionality constants relating  $S_{\text{in}}$  to  $\Omega_a$ ,  $S_q$  to  $\Omega_q$  and  $S_t$  to  $\langle a \rangle$  (see Fig. 15).

### 9. Output field statistics

For every drive amplitude  $S_{\text{in}}$ , the previous fit estimates the intracavity field  $\langle a \rangle$ , and hence  $\bar{n}$ . By acquiring histograms of the output field  $S_t$ , we now invert Eq. (D6) and retrieve  $\eta \simeq 7\%$ , a factor 2 larger than the previously estimated value. This deviation can be attributed to differences

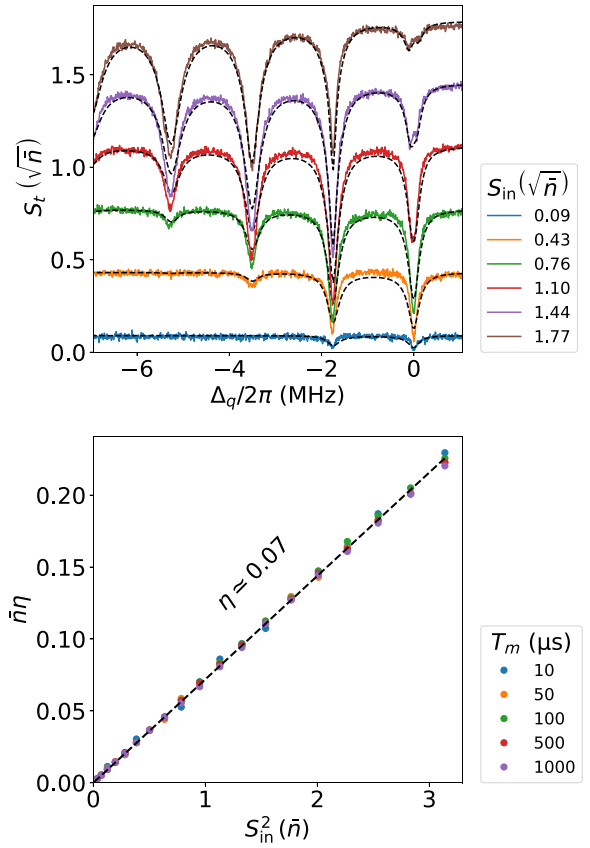


FIG. 15. Calibration of the detection efficiency  $\eta$ . (Top) Qubit spectroscopy showing photon-number splitting: data (solid lines) and fit (dashed lines). (Bottom) Product  $\bar{n}\eta$  computed using Eq. (D6) as a function of the square input signal  $S_{\text{in}}^2$  in units of photon number.

in the rf connections of the two samples. These values may be explained by lossy elements (two circulators, one Eccosorb filter, and two directional couplers) between the sample and the TWPA.

### APPENDIX E: BIT-FLIP TIME SIMULATIONS

We numerically simulate the dynamics of the memory described in Eq. (1) using the `mesolve` function imported from the QuTiP python package [35,36]. We run the simulation for three different values of  $g_2$  (or equivalently  $\kappa_2$ ). For each of these values, we sweep  $\epsilon_2$  in order to vary  $\bar{n} = |\alpha|^2$  in the range of 4 to 40 photons. We initialize the memory in the coherent state  $|\alpha\rangle$ , and fit the expectation value of the annihilation operator  $a$  to an exponentially decaying function. The extracted decay time corresponds to the bit-flip time. In Fig. 16, we display the computed bit-flip time as a function of the product  $\bar{n} \times (g_2/2\pi)^2$ , since it is a well-calibrated quantity in our experiment. The data lie in the vicinity of the simulation results for  $g_2/2\pi = 39$  kHz, thus confirming our calibration of  $g_2$ .

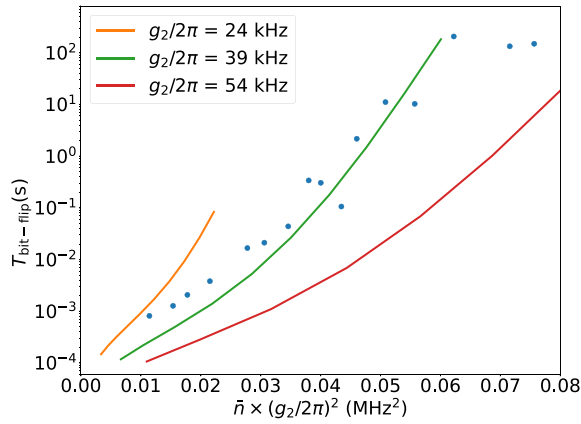


FIG. 16. Numerical simulations (solid lines) of the bit-flip time ( $y$  axis) for three values of  $g_2$  (labels) as a function of the number of photons in the memory  $\bar{n}$  multiplied by  $(g_2/2\pi)^2$  ( $x$  axis). The data (dots) from Fig. 4 of the main text qualitatively matches the simulations for  $g_2/2\pi = 39$  kHz, thus confirming our calibration of  $g_2$ .

[1] M. Dykman and M. Krivoglaz, Fluctuations in nonlinear systems near bifurcations corresponding to the appearance of new stable states, *Phys. A: Stat. Mech. Appl.* **104**, 480 (1980).

[2] J. Guckenheimer and P. Holmes, *Nonlinear Oscillations, Dynamical Systems, and Bifurcations of Vector Fields* (Springer New York, New York, NY, 1983), p. 1.

[3] I. Siddiqi, R. Vijay, F. Pierre, C. M. Wilson, M. Metcalfe, C. Rigetti, L. Frunzio, and M. H. Devoret, rf-Driven Josephson Bifurcation Amplifier for Quantum Measurement, *Phys. Rev. Lett.* **93**, 207002 (2004).

[4] P. Krantz, A. Bengtsson, M. Simoen, S. Gustavsson, V. Shumeiko, W. D. Oliver, C. M. Wilson, P. Delsing, and J. Bylander, Single-shot read-out of a superconducting qubit using a Josephson parametric oscillator, *Nat. Commun.* **7**, 11417 (2016).

[5] H. Mabuchi, Nonlinear interferometry approach to photonic sequential logic, *Appl. Phys. Lett.* **99**, 153103 (2011).

[6] J. Kerckhoff and K. W. Lehnert, Superconducting Microwave Multivibrator Produced by Coherent Feedback, *Phys. Rev. Lett.* **109**, 153602 (2012).

[7] P. R. Muppalla, O. Gargiulo, S. I. Mirzaei, B. P. Venkatesh, M. L. Juan, L. Grünhaupt, I. M. Pop, and G. Kirchmair, Bistability in a mesoscopic Josephson junction array resonator, *Phys. Rev. B* **97**, 024518 (2018).

[8] H. J. Carmichael, *Statistical Methods in Quantum Optics 2* (Springer Berlin Heidelberg, 2008), <https://link.springer.com/book/10.1007/978-3-540-71320-3>.

[9] Z. Leghtas, S. Touzard, I. M. Pop, A. Kou, B. Vlastakis, A. Petrenko, K. M. Sliwa, A. Narla, S. Shankar, M. J. Hatridge, M. Reagor, L. Frunzio, R. J. Schoelkopf, M. Mirrahimi, and M. H. Devoret, Confining the state of light to a quantum manifold by engineered two-photon loss, *Science* **347**, 853 (2015).

[10] M. Mirrahimi, Z. Leghtas, V. V. Albert, S. Touzard, R. J. Schoelkopf, L. Jiang, and M. H. Devoret, Dynamically protected cat-qubits: A new paradigm for universal quantum computation, *New J. Phys.* **16**, 045014 (2014).

[11] R. Lescanne, M. Villiers, T. Peronnin, A. Sarlette, M. Delbecq, B. Huard, T. Kontos, M. Mirrahimi, and Z. Leghtas, Exponential suppression of bit-flips in a qubit encoded in an oscillator, *Nat. Phys.* **16**, 509 (2020).

[12] C. Wang, C. Axline, Y. Y. Gao, T. Brecht, Y. Chu, L. Frunzio, M. H. Devoret, and R. J. Schoelkopf, Surface participation and dielectric loss in superconducting qubits, *Appl. Phys. Lett.* **107**, 162601 (2015).

[13] M. McEwen, *et al.*, Resolving catastrophic error bursts from cosmic rays in large arrays of superconducting qubits, *Nat. Phys.* **18**, 107 (2021).

[14] P. Campagne-Ibarcq, A. Eickbusch, S. Touzard, E. Zalusky-Geller, N. E. Frattini, V. V. Sivak, P. Reinhold, S. Puri, S. Shankar, R. J. Schoelkopf, L. Frunzio, M. Mirrahimi, and M. H. Devoret, Quantum error correction of a qubit encoded in grid states of an oscillator, *Nature* **584**, 368 (2020).

[15] A. Grimm, N. E. Frattini, S. Puri, S. O. Mundhada, S. Touzard, M. Mirrahimi, S. M. Girvin, S. Shankar, and M. H. Devoret, Stabilization and operation of a Kerr-cat qubit, *Nature* **584**, 205 (2020).

[16] R. Gautier, A. Sarlette, and M. Mirrahimi, Combined Dissipative and Hamiltonian Confinement of Cat Qubits, *PRX Quantum* **3**, 020339 (2022).

[17] R. Lescanne, L. Verney, Q. Ficheux, M. H. Devoret, B. Huard, M. Mirrahimi, and Z. Leghtas, Escape of a Driven Quantum Josephson Circuit into Unconfined States, *Phys. Rev. Appl.* **11**, 014030 (2019).

[18] L. Verney, R. Lescanne, M. H. Devoret, Z. Leghtas, and M. Mirrahimi, Structural Instability of Driven Josephson Circuits Prevented by an Inductive Shunt, *Phys. Rev. Appl.* **11**, 024003 (2019).

[19] M. Burgelman, P. Rouchon, A. Sarlette, and M. Mirrahimi, Structurally Stable Subharmonic Regime of a Driven Quantum Josephson Circuit, *Phys. Rev. Appl.* **18**, 064044 (2022).

[20] D. M. Pozar, *Microwave Engineering* (Wiley, 2012), 4th ed, <https://www.wiley.com/en-us/Microwave+Engineering,+4th+Edition-p-9780470631553>.

[21] S. M. Girvin, in *Quantum Machines: Measurement and Control of Engineered Quantum Systems (Les Houches Session XCVI)*, edited by M. Devoret, B. Huard, R. Schoelkopf, and L. F. Cugliandolo (Oxford University Press, 2014), p. 113.

[22] V. Y. Mylnikov, S. O. Potashin, G. S. Sokolovskii, and N. S. Averkiev, Dissipative phase transition in systems with two-photon drive and nonlinear dissipation near the critical point, *Nanomaterials* **12**, 2543 (2022).

[23] A. P. Vepsäläinen, A. H. Karamlou, J. L. Orrell, A. S. Dogra, B. Loer, F. Vasconcelos, D. K. Kim, A. J. Melville, B. M. Niedzielski, J. L. Yoder, S. Gustavsson, J. A. Formaggio, B. A. VanDevender, and W. D. Oliver, Impact of ionizing radiation on superconducting qubit coherence, *Nature* **584**, 551 (2020).

[24] L. Cardani, *et al.*, Reducing the impact of radioactivity on quantum circuits in a deep-underground facility, *Nat. Commun.* **12**, 2733 (2021).



- [25] J. Guillaud and M. Mirrahimi, Repetition Cat Qubits for Fault-Tolerant Quantum Computation, *Phys. Rev. X* **9**, 041053 (2019).
- [26] C. Chamberland, K. Noh, P. Arrangoiz-Arriola, E. T. Campbell, C. T. Hann, J. Iverson, H. Putterman, T. C. Bohdanowicz, S. T. Flammia, A. Keller, G. Refael, J. Preskill, L. Jiang, A. H. Safavi-Naeini, O. Painter, and F. G. Brandão, Building a Fault-Tolerant Quantum Computer using Concatenated Cat Codes, *PRX Quantum* **3**, 010329 (2022).
- [27] S. Krinner, N. Lacroix, A. Remm, A. D. Paolo, E. Genois, C. Leroux, C. Hellings, S. Lazar, F. Swiadek, J. Herrmann, G. J. Norris, C. K. Andersen, M. Müller, A. Blais, C. Eichler, and A. Wallraff, Realizing repeated quantum error correction in a distance-three surface code, *Nature* **605**, 669 (2022).
- [28] Google, Suppressing quantum errors by scaling a surface code logical qubit, *Nature* **614**, 676 (2023).
- [29] U. Vool, I. M. Pop, K. Sliwa, B. Abdo, C. Wang, T. Brecht, Y. Y. Gao, S. Shankar, M. Hatridge, G. Catelani, M. Mirrahimi, L. Frunzio, R. J. Schoelkopf, L. I. Glazman, and M. H. Devoret, Non-Poissonian Quantum Jumps of a Fluxonium Qubit due to Quasiparticle excitations, *Phys. Rev. Lett.* **113**, 247001 (2014).
- [30] R. Azouit, A. Sarlette, and P. Rouchon, in *2016 IEEE 55th Conference on Decision and Control (CDC)* (IEEE, 2016).
- [31] N. Bartolo, F. Minganti, W. Casteels, and C. Ciuti, Exact steady state of a kerr resonator with one- and two-photon driving and dissipation: Controllable Wigner-function multimodality and dissipative phase transitions, *Phys. Rev. A* **94**, 033841 (2016).
- [32] S. Puri, S. Boutin, and A. Blais, Engineering the quantum states of light in a Kerr-nonlinear resonator by two-photon driving, *npj Quantum Inf.* **3**, 18 (2017).
- [33] A. Barchielli and M. Gregoratti, *Quantum Trajectories and Measurements in Continuous Time* (Springer Berlin Heidelberg, 2009), <https://link.springer.com/book/10.1007/978-3-642-01298-3>.
- [34] A. Tilloy, Exact signal correlators in continuous quantum measurements, *Phys. Rev. A* **98**, 010104 (2018).
- [35] J. Johansson, P. Nation, and F. Nori, Qutip: An open-source python framework for the dynamics of open quantum systems, *Comput. Phys. Commun.* **183**, 1760 (2012).
- [36] J. Johansson, P. Nation, and F. Nori, Qutip 2: A python framework for the dynamics of open quantum systems, *Comput. Phys. Commun.* **184**, 1234 (2013).